Concurrent design and flight mission optimization of morphing airborne wind energy wings

Urban Fasel*, Paolo Tiso†, Dominic Keidel‡, and Paolo Ermanni§
ETH Zurich, 8092 Zurich, Switzerland

Morphing wings are expected to have transformative impact on future transportation and energy systems. To enable analysis and optimization of morphing wings, efficient numerical models are critically important. In this work, we present an accurate and tractable reduced-order model embedded in a genetic algorithm based optimization framework. The modeling and optimization framework allows concurrent aero-structural design and flight trajectory optimization of morphing wings considering complete flight missions. The approach is demonstrated on a camber-morphing wing airborne wind energy (AWE) system. The system's power production capability is improved by enabling wing shape changes and thus adaptation of the aerodynamic properties through morphing at different flight conditions and operating modes. The results of this study highlight the potential of the proposed modeling and optimization approach: 1) the power production capability of the investigated AWE system is improved by 46.0% compared to a sequentially optimized wing design, and 2) by exploiting camber-morphing to adapt the aerodynamic properties of the wing at different flight conditions, the power production is further increased by 7.8%.

Nomenclature

$\boldsymbol{A}$, $\boldsymbol{B}$	aerodynamic influence coefficient matrix	c_{Roll}	roll coefficient
A	wing area	$\boldsymbol{F}$	external force vector acting on wing structure
$a_{s,cmd}$	lateral acceleration command	$\boldsymbol{F}_A$	forces acting on rigid aircraft
$\boldsymbol{C}_{Act}$	aircraft actuator inputs	$\boldsymbol{F}_{DS}$	generalized force vector dynamic system
C_T	ground station controller input	F_G	gravitational force
$\boldsymbol{c}_p$	pressure coefficient matrix	F_L	lift force
c_D	drag coefficient	$\boldsymbol{F}_T$	forces acting on tether
c_L	lift coefficient	$\boldsymbol{f}$	external force vector acting on wing structure

*Ph.D. Candidate, CMASLab, ETH Zurich, 8092 Zurich, Member AIAA (faselu@ethz.ch)
†Senior Scientist, Institute for Mechanical Systems, ETH Zurich, 8092 Zurich
‡Ph.D. Candidate, CMASLab, ETH Zurich, 8092 Zurich, Member AIAA
§Professor, CMASLab, ETH Zurich, 8092 Zurich, Member AIAA

	in modal coordinates
f_W	wind speed distribution probability
$\boldsymbol{K}$	structural stiffness matrix
$\widetilde{\boldsymbol{K}}$	structural modal stiffness matrix
L_1	distance between aircraft and reference point
l_t	length tether
$\boldsymbol{M}$	mass matrix
$\boldsymbol{M}_A$	moments acting on rigid aircraft
$\boldsymbol{M}_{DS}$	generalized mass matrix dynamic system
M_a, M_s	degrees of freedom aerodynamic and structural model
m_a	morphing actuation level
$\boldsymbol{n}$	aerodynamic mesh panel normal matrix
N	number of modes
P_A	average power production
$\bar{P}$	average annual power production
$\boldsymbol{q}$	structural modal amplitude vector
r	radius L_1 control
$\boldsymbol{r}_A$	rigid aircraft position
$\boldsymbol{r}_T$	tether particle position
$\boldsymbol{u}$	structural displacement vector
$\boldsymbol{V}$	flight velocity matrix
V_p	tilted plane projected velocity
$\boldsymbol{V}_w$	wind velocity
$\boldsymbol{v}_A$	aircraft kinematic velocity
$\boldsymbol{v}_T$	tether kinematic velocity
$\boldsymbol{X}$	flight state vector
$\boldsymbol{X}_T$	tether parameters vector
$\boldsymbol{y}$	dynamic state vector
α	angle of attack
$\boldsymbol{\alpha}_A$	aircraft Euler angles
γ	aircraft elevation angle
δ	tether opening angle
η	guidance controller angle
η_m	maneuvering related losses
θ_c	flight path circumferential angle
κ	elevation angle
$\boldsymbol{\mu}$	panel method doublet strength vector
$\boldsymbol{\sigma}$	panel method source strength vector
$\boldsymbol{\phi}$	structural expansion basis vector
ϕ	aircraft roll angle
$\boldsymbol{\Psi}$	structural expansion basis matrix
$\boldsymbol{\omega}_A$	aircraft angular velocity
ω_g	ground station angular velocity
ω_{v_i}	structural eigenfrequency

I. Introduction

Morphing wings have the potential to increase the performance of flight systems by adapting their aerodynamic properties to different flight conditions and operating modes [1, 2]. This is specifically beneficial for flight systems covering large operating regimes. To comprehensively predict system-level performance gains achieved by morphing, the application of detailed aeroelastic modeling and optimization methods considering complete flight missions is essential. Recent studies, however, mainly focus on 1) detailed morphing mechanism conceptual design without considering complete flight mission and system-level objectives [3–7] or on 2) high-fidelity modeling based optimization, not considering specific morphing mechanisms [8–10]. This work extends on the conceptual design studies, applying a camber-morphing wing to an airborne wind energy (AWE) system and conducting concurrent design

and complete flight mission optimizations. A high level objective in terms of average power production is defined, allowing to truly quantify the performance gains achieved through morphing.

AWE is a promising technology that aims to extract power from high altitude winds using tethered aircraft [11]. The AWE concept considered in this study is the ground-based power generation concept [12]. In this concept, tethered aircraft fly crosswind trajectories and use a substantial part of the produced aerodynamic lift to drive a ground-based generator via a tether. The power production consists of two distinct operating modes, namely the traction and retraction phase. In the traction phase, the aircraft is reeling out the tether from a winch, thereby driving the generator and producing power. After reaching a predefined maximum tether length, the aircraft is pulled back by the generator in the retraction phase, reaching the initial tether length and thus resetting the system for the next cycle. The traction and retraction operating modes differ drastically: in the traction phase, maximum power is produced by operating the aircraft at large incidence and high lift forces, whereas in the retraction phase, the force on the tether is minimized by flying at low lift and drag coefficients to reduce the required reel-in power [11]. Therefore, AWE is a particularly compelling application to employ morphing wings, which have the potential to operate with high effectiveness in multiple conditions. Morphing wings can change their aerodynamic shape (e.g. the camber of the airfoil), and thus lift distribution, continuously along the span, thereby offering the possibility to maneuver and simultaneously adapt to different flight conditions and wind speeds. The major challenge of applying morphing to AWE is however represented by the high aerodynamic loads encountered: the wing is required to be extremely stiff to withstand these loads while still being compliant enough to achieve the desired shape adaptability. Therefore, to quantify and fully exploit the potential of applying morphing to AWE, accurate and efficient complete flight mission aeroservoelastic models are required, concurrently considering flight dynamic and aeroelastic effects.

Initial studies on the aero-structural modeling and optimization of morphing wings for AWE have been conducted by the authors [13, 14]. In [13], a static aeroelastic analysis of an AWE morphing wing was conducted and the aerodynamic shape, the structural design, and the composite layup of the wing were concurrently optimized using an evolutionary algorithm. The results of the study highlighted the benefit of concurrently optimizing the aerodynamic and structural design of an AWE morphing wing compared to sequentially optimizing the single disciplines. However, the study did not consider a specific flight trajectory and flight dynamic effects. In [14], the aeroelastic simulation model was extended to consider the coupled flight dynamics and aeroelasticity of the morphing wing AWE system. Model order reduction techniques were introduced, allowing to run real-time simulations of the coupled dynamics. A particularly interesting feature of the introduced reduced-order modeling (ROM) technique were the low offline cost: the computational cost to build the ROM is low, thus allowing to efficiently perform multidisciplinary design optimizations where the ROM needs to be rebuild in each iteration.

This study builds on the findings of [13] and [14], presenting a modeling and optimization framework able to run concurrent complete flight mission and morphing mechanism design optimization. The approach is to use the

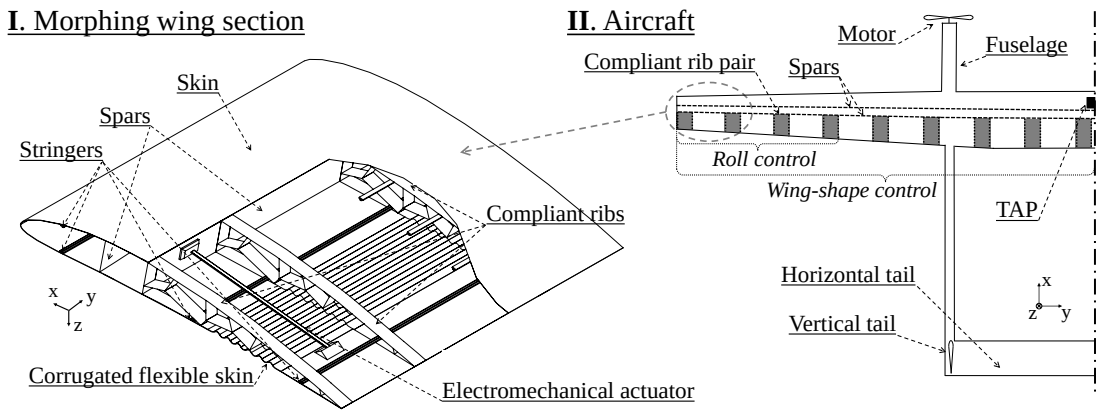

Figure 1 Aircraft configuration and morphing wing section.

ROM introduced in [14] to concurrently optimize the AWE flight mission (trajectory and control parameters) with the structural and aerodynamic design parameters of a camber-morphing wing. The procedure is thus an extension of the optimization framework introduced in [13], adding the controls and trajectory design parameters to the aero-structural optimization. In this study, the objective to be maximized is the mission performance of the morphing wing, defined as the average annual power production of the AWE system. Multiple optimizations are performed, highlighting two main findings regarding the optimization of the mission performance of a morphing wing: 1) the performance can be increased by concurrently optimizing the wing design and flight mission parameters compared to a sequential approach, and 2) the performance can be increased using camber-morphing to adapt the wing shape and spanwise lift distribution at different wind speeds and operating modes.

In the following section, the aircraft and morphing concept is presented in detail. In Section III, the modeling approach is introduced, followed by the optimization method in Section IV. Finally, the results of the optimizations are discussed in Section V.

II. AWE aircraft and morphing concept

The aircraft concept used in this study is based on the AWE aircraft developed by ftero at ETH Zurich [15, 16]. The aircraft configuration and the morphing concept are depicted in Figure 1. The aircraft comprises of a carbon fiber reinforced plastic (CFRP), high aspect ratio, high-lift wing and two electric motors - mounted on the two fuselages - allowing vertical take-off and landing (VTOL). The stabilizer consists of a horizontal all-moving tail and two vertical stabilizers positioned at the rear end of the fuselages. The tether attachment point (TAP) is located close to the center of gravity of the aircraft, reducing the pitching moment induced by the tether force.

The camber-morphing concept considered in this study relies on compliant ribs adopted from the work of Molinari et al. [17], driven by electromechanical actuators proposed by Keidel et al. [16, 18], and first applied to AWE wings

by the authors [13]. With the proposed camber-morphing concept, a variation in local lift coefficient is achieved by activating the actuators and thereby changing the camber of the wing profiles. The morphing wing consists of truss-like polylactide (PLA) compliant ribs, which guide the deformation to aerodynamically optimized shapes and provide the required stiffness. The mechanical energy to deform the structure is provided by electromechanical actuators. On the lower side of the wing, a corrugated laminate allows the overall length of the profile to change, thus permitting to achieve the required deformation with comparatively low energy [4, 19, 20].

In the case of the aircraft concept developed by ftero, the outermost part of the wing comprises of the camber-morphing section and is used for roll-control of the aircraft, replacing conventional ailerons. In this study, the morphing section is extended to allow camber changes along the complete wingspan. The four outermost actuators are still used for roll-control, however, all nine actuators per half span are used to adapt the wing shape at different flight conditions. Apart from adapting the wing shape at different wind speeds and operating modes, the extended camber morphing capabilities can also be exploited to alleviate gust loads. Thereby, the effects of possible disturbances can be directly mitigated at the aircraft by morphing the wing, potentially improving the power production capabilities of the AWE system. Thus, the morphing can be used for roll-control, wing shape adaptation at different flight conditions, and gust load alleviation.

III. Modeling approach

To perform complete flight mission analysis of the morphing AWE wing, a coupled flight dynamic and aeroelastic model including a flight controller is introduced. The modeling framework relies on alternately solving a fluid structure interaction (FSI) model of the morphing wing and a dynamic system model consisting of the rigid aircraft-, tether-, and ground station-dynamics. The schematic of the simulation is shown in Figure 2. This co-simulation approach is applicable to the problem at hand, owing to the large frequency separation between the natural modes of the rigid-body degrees of freedom (below 1 Hz) and the elastic degrees of freedom of the wing (above 10 Hz). This frequency separation is generally found in all comparably stiff aircraft, but would not be present in larger, more flexible aircraft [21, 22], where a fully coupled monolithic simulation would be the alternative approach. The big advantage of the co-simulation approach is that the AWE system dynamics and the wing aeroelastic simulation can be modeled separately, allowing to apply model order reduction techniques to the computationally expensive aeroelastic model. The numerical model is introduced in detail in [14]. For completeness, the model is summarized in the following.

A. Fluid-structure interaction

The FSI model consists of a 3-D structural finite element model with M_s degrees of freedom to assess the structural behavior, coupled with a 3-D panel method [23, 24] with M_a panels to calculate the aerodynamic characteristics of the wing. For the reference aircraft, the structural and aerodynamic system have approximately $M_s = 61'000$ and $M_a = 656$

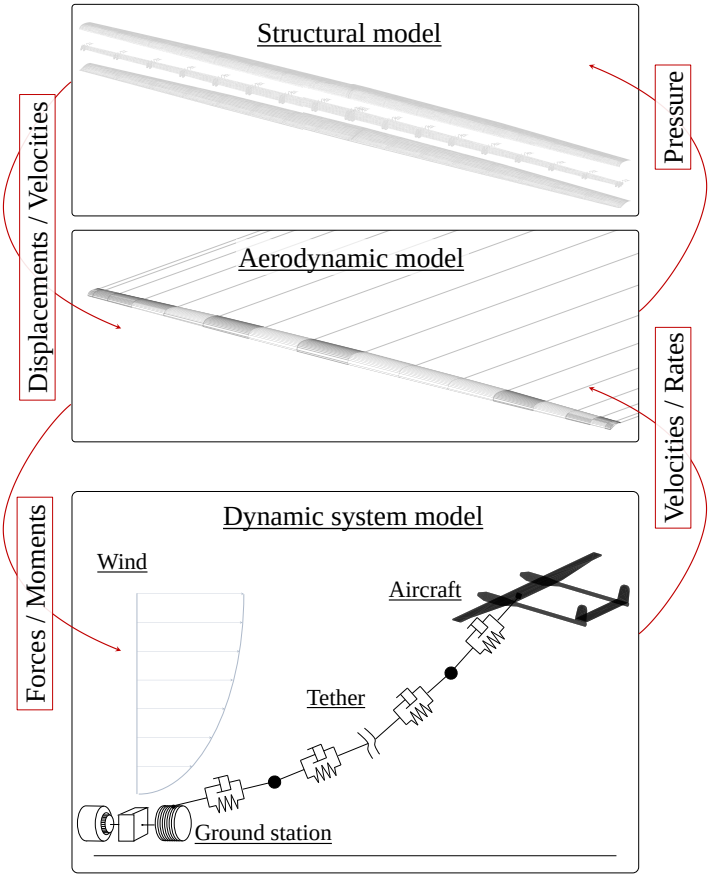

Figure 2 Coupling procedure of the dynamic system model with the aerodynamic and structural model. Top: Exploded view of the structural model highlighting the modeling detail of the compliant structure based morphing wing. Center: Aerodynamic model. Bottom: Dynamic system model consisting of aircraft, tether, and ground station.

degrees of freedom. However, the size of the structural model changes within this study, as the model is rebuild for each individual wing design in the optimization introduced in Section IV. Two distinct interpolation methods are applied to transfer the structural displacements and the aerodynamic forces between the structural and the aerodynamic mesh and vice versa, described in Subsection 3. The focus of this study lies in particular on the modeling of the main wing and the wing's morphing capability, thus, the fuselage and empennage are modeled as rigid bodies owing to their high stiffness compared to the morphing wing. Furthermore, the aerodynamic characteristics of the all-moving tail and the vertical stabilizer are modeled independently from the main wing, simplifying the modeling and accelerating the computation of the simulation. The FSI model has been validated against the model introduced in [4], which in turn has been successfully validated in a previous study against wind tunnel tests [25].

1. Structural model

The CFRP wing skin and PLA internal structure are modeled using plate elements, the stringers are modeled as beam elements, and the corrugated skin is modeled using a substitute plate model [26, 27]. A zero displacement boundary condition is imposed at the wing root where the tether attachment point is located on the aircraft. The mesh of the wing is generated in MATLAB and the mass- and stiffness-matrices $\boldsymbol{M}, \boldsymbol{K} \in \mathbb{R}^{M_s \times M_s}$ are obtained using the commercial FE software Nastran [28]. The linearized equations of motion of the finite element model are given by:

$$\boldsymbol{K}\boldsymbol{u} = \boldsymbol{F}, \tag{1}$$

where $\boldsymbol{u} \in \mathbb{R}^{M_s}$ are the displacements and $\boldsymbol{F} \in \mathbb{R}^{M_s}$ are the external loads. Compared to the dynamic model introduced in [14], the model in this study assumes quasi-steady deformations of the structure. This is motivated by the smooth trajectories and comparably slow maneuvers of the aircraft and therefore negligible effects of the dynamics introduced by the structure on the flown trajectory and produced power.

The computational efficiency of the simulation is increased by applying a model order reduction technique, relying on a mode superposition method [29]. The $N_v = 8$ first vibration modes* in combination with the $N_m = 3$ morphing modes (activating the four outermost left actuators, the four outermost right actuators, and all the actuators over the full span according to the desired wing shape change) define the chosen reduction basis. The vibration modes $\boldsymbol{\phi}_{v_i} \in \mathbb{R}^{M_s}$ are obtained by solving the generalized eigenvalue problem associated to free vibrations, namely for the i^{th} mode: $(\boldsymbol{K} - \omega_{v_i}^2 \boldsymbol{M})\boldsymbol{\phi}_{v_i} = \boldsymbol{0}$, with the corresponding eigenfrequency ω_{v_i}. The morphing modes $\boldsymbol{\phi}_{m_i} \in \mathbb{R}^{M_s}$ are computed by solving the static equation of motion with the morphing actuation forces $\boldsymbol{F}_{m_i}$ acting as external loads, as: $\boldsymbol{\phi}_{m_i} = \boldsymbol{K}^{-1}\boldsymbol{F}_{m_i}$.

The structural displacements $\boldsymbol{u}$ can then be approximated as follows:

$$\boldsymbol{u} \approx \begin{bmatrix} \boldsymbol{\Psi}_v & \boldsymbol{\Psi}_m \end{bmatrix} \begin{bmatrix} \boldsymbol{q}_v \\ \\ \boldsymbol{q}_m \end{bmatrix} = \boldsymbol{\Psi}\boldsymbol{q}, \tag{2}$$

where $\boldsymbol{\Psi}_v \in \mathbb{R}^{M_s \times N_v}$ is an orthonormal basis containing the N_v vibration modes $\left[\boldsymbol{\phi}_{v_1}, ..., \boldsymbol{\phi}_{v_i}, ...\boldsymbol{\phi}_{v_{N_v}}\right]$, $\boldsymbol{\Psi}_m \in \mathbb{R}^{M_s \times N_m}$ are the three morphing deformation modes $\left[\boldsymbol{\phi}_{m_1}, \boldsymbol{\phi}_{m_2}, \boldsymbol{\phi}_{m_3}\right]$, $\boldsymbol{q}_v \in \mathbb{R}^{N_v}$ and $\boldsymbol{q}_m \in \mathbb{R}^{N_m}$ are the vibration and morphing modal amplitudes, and $\boldsymbol{\Psi} \in \mathbb{R}^{M_s \times N}$ and $\boldsymbol{q} \in \mathbb{R}^{N}$ are the total expansion basis respectively the total modal amplitude vector with $N = N_v + N_m$. By inserting formula 2 in 1 and by adopting a Galerkin projection, the reduced equations of motion are given by [30]:

$$\widetilde{\boldsymbol{K}}\boldsymbol{q} = \boldsymbol{\Psi}^{\boldsymbol{T}}\boldsymbol{F} = \boldsymbol{f}, \tag{3}$$

*The number of vibration modes N_v is determined by a convergence study, running circular flight test cases with the reference aircraft discussed in [14].

with $\boldsymbol{f} \in \mathbb{R}^N$ being the external forces in modal coordinates (comprising the aerodynamic and morphing actuator forces) and where the modal matrix $\widetilde{\boldsymbol{K}} = \boldsymbol{\Psi}^{\boldsymbol{T}} \boldsymbol{K} \boldsymbol{\Psi} \in \mathbb{R}^{N \times N}$ is only calculated once for each wing design. In terms of efficiency, a speed-up factor of 12′000 is achieved with the reduced-order structural model.

2. Aerodynamic model

The aerodynamic characteristics of the wing are calculated using a potential flow-based 3-D panel method [23, 24], owing to its ability to compute surface pressures of volumetric bodies and to its capability of accounting for thickness and camber changes of the wing. Accounting for these effects is necessary to achieve a satisfactory accuracy when analyzing camber-morphing wings, and thus dictates the choice of the aerodynamic analysis method. The specific implementation relies on a source-doublet formulation, which solves the Laplace equation in terms of the velocity potential for a Dirichlet boundary condition on the wing, and enforces the Kutta condition at the trailing edge. The wing is discretized with surface panel elements and a flat wake is shed by the trailing edge upper and lower panels. A flat wake instead of a helical shaped wake without further tracking the trajectory of the shed wake panels is considered, owing to the comparably low unsteadiness of the flow around the aircraft for the investigated trajectory and the negligible influence on the downwash velocity on the lifting surface from the helical shaped wake [14]. The resulting system of equations is given by:

$$\boldsymbol{A}(\boldsymbol{u})\boldsymbol{\mu} + \boldsymbol{B}(\boldsymbol{u})\boldsymbol{\sigma} = \boldsymbol{0}, \tag{4}$$

where $\boldsymbol{A}(\boldsymbol{u}), \boldsymbol{B}(\boldsymbol{u}) \in \mathbb{R}^{M_a \times M_a}$ are the configuration dependent doublet and source aerodynamic influence coefficient matrices (AIC), $\boldsymbol{\mu} \in \mathbb{R}^{M_a}$ is the doublet strength, and $\boldsymbol{\sigma} \in \mathbb{R}^{M_a}$ is the source strength [23]. It is important to notice that $\boldsymbol{A}$ and $\boldsymbol{B}$ are functions of the current deformed geometry $\boldsymbol{u}$. For the moderate wing deformations of the aircraft designs investigated in this study, the wing bending and rotation would only marginally change the AIC and could therefore be kept constant. However, the wing cambering can significantly change the AIC. Therefore, they should be recomputed at every time step. The detailed derivation of the doublet and source AIC is described in [23]. The source strength $\boldsymbol{\sigma}$ is directly obtained enforcing the Dirichlet boundary condition, knowing the panel normal $\boldsymbol{n} \in \mathbb{R}^{M_a \times 3}$ and the flight velocity $\boldsymbol{V} \in \mathbb{R}^{M_a \times 3}$ seen by each panel, with $\boldsymbol{\sigma} = -\boldsymbol{n} \cdot \boldsymbol{V}$. The system is solved for the doublet strength $\boldsymbol{\mu} = \boldsymbol{A}^{-1}\boldsymbol{B}(\boldsymbol{n} \cdot \boldsymbol{V})$, which is then used to calculate the total panel velocities and finally the pressure coefficient $\boldsymbol{c}_p \in \mathbb{R}^{M_a}$. The aerodynamic lift is calculated by integrating the pressure field over the wing surface. The induced drag c_{D_i} is estimated using an extended lifting line method, using the spanwise local lift coefficients assessed by the 3-D panel method [23]. Due to the inviscid nature of the panel method, the viscous drag c_{D_v} of the wing is introduced in a preprocessing step by a nonlinear extended lifting line, using XFOIL to calculate the 2-D aerodynamic characteristics of the airfoil [23, 31–33]. The viscous drag is only calculated for the undeformed wing. This can be justified by the small variations in c_{D_v} due to wing deformations and the very high lift coefficient flight conditions, leading to $c_{D_i} > c_{D_v}$. In the same preprocessing

step, the stall angle of attack is assessed. This is especially important as the aircraft operates at large angles of attack to maximize power production. Therefore, the maximum lift coefficient needs to be assessed to avoid overestimation of the system's power production capabilities. In [34], different methods to rapidly evaluate the low-speed 3-D maximum lift coefficient are compared. The critical section method (CSM) [35] shows best agreement with wind tunnel tests for unswept wings and is therefore used in this study. The 3-D stall angle of attack is thus estimated as the minimum angle where the spanwise local lift coefficient is equal to the maximum local 2-D lift coefficient.

Similar to the structural problem, model order reduction techniques are applied to the aerodynamic model to increase its computational efficiency. Instead of recalculating the AIC matrix $\boldsymbol{A}$ and $\boldsymbol{B}$ at each time step, a Taylor expansion of the AIC in the direction of the structural vibration and morphing modes is implemented (a linearization only in the direction of the morphing modes would not significantly reduce the accuracy of the model considering the moderate wing deformations of the specific wing designs investigated in this study):

$$\boldsymbol{A} \approx \boldsymbol{A}_0 + \sum \boldsymbol{A}_i q_i, \tag{5}$$

where $\boldsymbol{A}_0$ is the AIC for the initial statically deformed wing, and $\boldsymbol{A}_i$ is the AIC of the i^{th} reduction base shape.[†] The system of equation 4 needs to be inverted, thus equation 5 still needs to be factorized at every time step. For this, it is possible to employ the theorem of Miller [36], which provides an exact expression of the inverse of the sum of two arbitrary non singular square matrices. Applied to $\boldsymbol{A}$, the calculation of the inverse can be performed by computing the inverse of $\boldsymbol{A}_0$, and by performing simple matrix multiplications:

$$\boldsymbol{A}^{-1} = \boldsymbol{A}_0^{-1} - \frac{1}{1 - \mathrm{tr}(\sum \boldsymbol{A}_i q_i \boldsymbol{A}_0^{-1})} \boldsymbol{A}_0^{-1} \sum \boldsymbol{A}_i q_i \boldsymbol{A}_0^{-1}. \tag{6}$$

With the reduced-order aerodynamic model, a speed-up factor of 80 is achieved. Coupled with the structural simulation, a total speed up factor of 180 is achieved, clearly highlighting the potential of the proposed reduction method.

3. Interpolation

Two distinct interpolation methods are applied to transfer the displacements and aerodynamic forces between the structural and the aerodynamic mesh and vice versa. The displacements of the structural mesh are interpolated using the thin plate spline method [37–39], whereas the aerodynamic forces are interpolated using an inverse distance weighting method [40]. The interpolation of the aerodynamic loads could be computed by multiplying the transpose of the thin plate spline matrix with the aerodynamic load vector, without the need to introduce the inverse distance weighting method. However, the drawback of this approach are large oscillations in the interpolated loads [41], therefore, the method is not suitable and the inverse distance weighting approach [40] is applied instead.

[†]The AIC for the different reduction base shapes are calculated using forward difference: $\boldsymbol{A_i} = \frac{\boldsymbol{A}(\boldsymbol{\phi}_i \delta q_i) - \boldsymbol{A}_0}{\delta q_i}$.

At each time step of the FSI, the aerodynamic loads and the structural displacements are solved iteratively, until convergence criteria based on modal amplitude and pressure distribution are satisfied. After convergence, the computed aerodynamic forces $\boldsymbol{F}_A$ and moments $\boldsymbol{M}_A$ are transferred to the dynamic system model. The FSI procedure is summarized in Algorithm 1.

Algorithm 1. Assess aerodynamic forces and moments acting on the aircraft using the FSI model

Input: Aircraft state and actuator inputs: $\boldsymbol{v}_A$, $\boldsymbol{\omega}_A$, $\boldsymbol{q}$, $\boldsymbol{C}_{Act}$
Output: Aircraft forces and moments: $\boldsymbol{F}_A$, $\boldsymbol{M}_A$
procedure FSI($\boldsymbol{v}_A$, $\boldsymbol{\omega}_A$, $\boldsymbol{q}$, $\boldsymbol{C}_{Act}$)
  while not converged **do**
    $\boldsymbol{f} = \boldsymbol{f}(\boldsymbol{v}_A, \boldsymbol{\omega}_A, \boldsymbol{q}, \boldsymbol{C}_{Act})$ ▷ Compute aerodynamic and actuator loads $\boldsymbol{f}$ in modal coordinates
    $\boldsymbol{q} = \widetilde{\boldsymbol{K}}^{-1}\boldsymbol{f}$ ▷ Compute modal amplitudes $\boldsymbol{q}$
  end while
  $\boldsymbol{F}_A = \boldsymbol{F}_A(\boldsymbol{f})$, ▷ Compute forces and moments $\boldsymbol{F}_A$, $\boldsymbol{M}_A$ acting on aircraft
  $\boldsymbol{M}_A = \boldsymbol{M}_A(\boldsymbol{f})$
end procedure

B. Dynamic system model

The FSI is coupled with a dynamic system model to allow complete flight mission simulation. The dynamic system model consists of a six degrees of freedom model representing the aircraft [42], a multiple particle system representing the tether [43], and a single degree of freedom model of the ground station, consisting of the winch, the gearbox, and the generator [44], shown in Figure 3. The wind speed variation as a function of the altitude is considered with a logarithmic law [45]. A detailed description of the dynamic system model can be found in [14]. The resulting dynamic system has $d_{\mathrm{DS}} = 22$ degrees of freedom and is given by:

$$\boldsymbol{M}_{DS}\dot{\boldsymbol{y}} = \boldsymbol{F}_{DS} = [\boldsymbol{F}_A, \boldsymbol{M}_A, \boldsymbol{F}_T]^T, \tag{7}$$

where $\boldsymbol{M}_{DS} \in \mathbb{R}^{d_{\mathrm{DS}} \times d_{\mathrm{DS}}}$ is the generalized mass matrix, $\boldsymbol{F}_{DS} \in \mathbb{R}^{d_{\mathrm{DS}}}$ is the generalized force vector (with $\boldsymbol{F}_A$, $\boldsymbol{M}_A$ being the aerodynamic forces and moments acting on the aircraft calculated using the FSI, and $\boldsymbol{F}_T$ the forces acting on the tether), and $\boldsymbol{y}$, $\dot{\boldsymbol{y}} \in \mathbb{R}^{d_{\mathrm{DS}}}$ is the dynamic state vector and its time derivative. Equation 7 can be reformulated as: $\dot{\boldsymbol{y}} = \boldsymbol{M}_{DS}^{-1}\boldsymbol{F}_{DS} = f(\boldsymbol{y}, \boldsymbol{X}, t)$, indicating the functional dependency of $\dot{\boldsymbol{y}}$ on the dynamic state vector $\boldsymbol{y}$ and the flight state vector $\boldsymbol{X} \in \mathbb{R}^{d_{\mathrm{DS}}}$. The dynamic state vector $\boldsymbol{y}$ consists of the aircraft kinematic and angular velocity $\boldsymbol{v}_A$, $\boldsymbol{\omega}_A \in \mathbb{R}^3$, the tether particle velocity $\boldsymbol{v}_T \in \mathbb{R}^{15}$, and the ground station angular velocity ω_g: $\boldsymbol{y} = (\boldsymbol{v}_A, \boldsymbol{\omega}_A, \boldsymbol{v}_T, \omega_g)^T$. The flight state vector $\boldsymbol{X}$ consists of the aircraft and tether particle position $\boldsymbol{r}_A \in \mathbb{R}^3$ and $\boldsymbol{r}_T \in \mathbb{R}^{15}$, the Euler angles $\boldsymbol{\alpha}_A \in \mathbb{R}^3$, and the wind speed v_W: $\boldsymbol{X} = (\boldsymbol{r}_A, \boldsymbol{r}_T, \boldsymbol{\alpha}_A, v_W)^T$. The numerical integration of the dynamic system over time is computed using an explicit scheme, directly calculating the state at t_{i+1} from the state variables at t_i. The MATLAB variable-step

Adams-Bashforth-Moulton PECE solver ODE113 was found to outperform other solvers in terms of simulation time and is therefore used for the numerical integration. The numerical integration process is depicted in Figure 3.

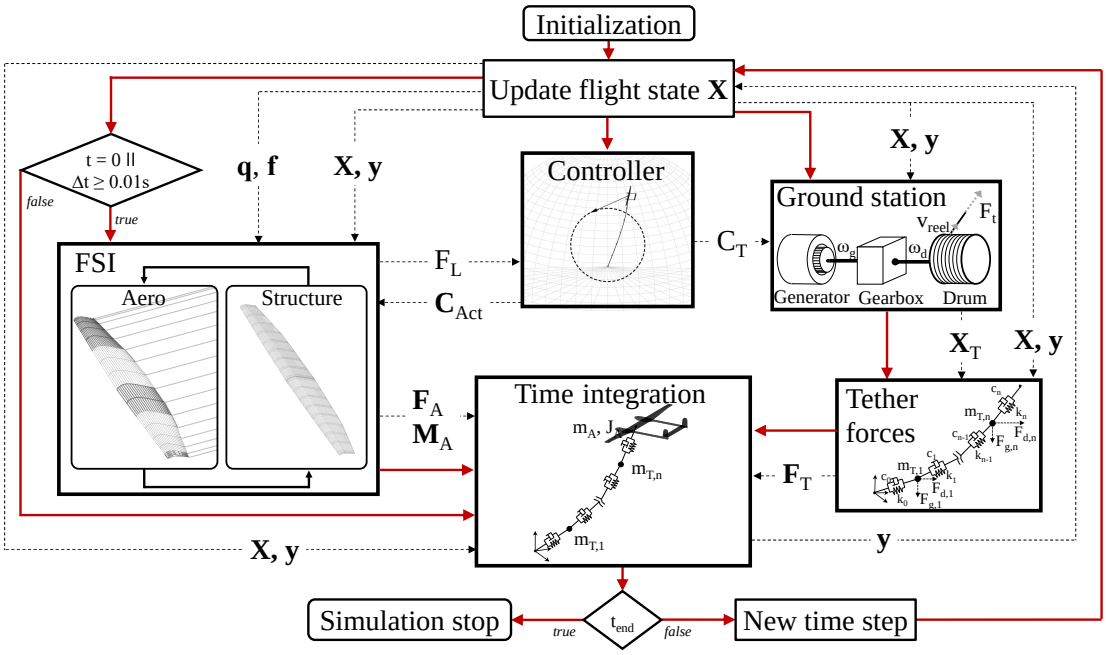

Figure 3 Coupled flight dynamic and aeroelastic model.

The model is initialized and the flight state vector $\boldsymbol{X}$ and the dynamic state vector $\boldsymbol{y}$ are passed to the flight controller, the FSI, the ground station and tether module, and to the time integration. The flight controller, described in detail in the following section, sets the morphing wing actuator inputs of the aircraft $\boldsymbol{C}_{Act}$ and the controller input of the ground station C_T. Additionally to the flight state vector and the actuator inputs, the aerodynamic force vector in modal coordinates $\boldsymbol{f}$ and the modal amplitudes $\boldsymbol{q}$ from the preceding FSI step are passed to the FSI module. In the FSI module, the forces and moments $\boldsymbol{F}_A$ and $\boldsymbol{M}_A$ acting on the aircraft are calculated. The sample time of the FSI is set to $\Delta t_{FSI} = 0.01$ s, and the maximum overall time step size of the dynamic system solver is set to $\Delta t_{DS} = 0.01$ s. In the ground station module, the produced power is assessed and the tether parameters $\boldsymbol{X}_T$, consisting of the spring and damping constant and the tether segment mass and length, are updated. In the tether forces module the loads acting on the particles $\boldsymbol{F}_T$ are assessed. The calculated loads and moments $\boldsymbol{F}_A$, $\boldsymbol{M}_A$, and $\boldsymbol{F}_T$ are passed to the time integration and the dynamic state vector $\boldsymbol{y}$ is advanced. The flight state is then updated and the next iteration is initialized.

C. Flight control

To perform complete flight mission analysis, a flight controller consisting of an aircraft and ground station controller is included in the dynamic simulation, enabling the tethered aircraft to follow predefined trajectories. The control strategy is based on a modified state-of-the art flight controller for fixed wing aircraft and was first adopted for AWE in

[46]. The aircraft follows a circular trajectory and the ground station is periodically reeling out (traction phase) and reeling in (retraction phase) the tether. A circular trajectory with a single flight loop is chosen in this study for its simplicity. Flying a different trajectory and flying multiple traction loops before retracting the aircraft could potentially increase the average power production of the AWE system but is still object of ongoing research [11, 47–49]. The guidance is decomposed by separately controlling the radial and lateral dynamics of the aircraft. The radial dynamics are set by the winch, pitch, and morphing controller, whereas the lateral dynamics are set by the roll controller. In yaw direction, the aircraft is stable and no active control is implemented. Similar control strategies for rigid wing AWE aircraft can be found in [50] and [51].

1. Radial dynamics

The dynamics of the aircraft in radial direction are controlled by the winch and by the elevator of the aircraft. The winch controller periodically reels out and reels in the tether, and the pitch controller simultaneously adapts the angle of attack of the aircraft. The aircraft accelerates in downward flight when the gravity acts in flight direction: in this condition, maximum flight speeds are reached and consequently maximum power can be produced. Therefore, the tether is reeled out in downward flight, followed by reeling in as soon as the upward flight is initiated, where the gravity points in the opposite of the flight direction and the aircraft decelerates. Likewise, the angle of attack is set to its specific operating point when reeling out, not exceeding the precomputed stall angle of attack, and decreased when reeling in, minimizing the power consumption of the winch in the retraction phase. Both the desired tether length and angle of attack are set by Fourier series on the desired flight path of the variable θ_c, representing the aircraft's circumferential angle on the flight circle, depicted in Figure 4. The Fourier series describing the desired tether length l_t and angle of attack α are defined as follows:

$$l_t(\theta_c) = l_{t,0} - l_{t,1}\cos(\theta_c + \theta_{1,l}) - l_{t,2} \cdot \cos(2(\theta_c + \theta_{2,l})), \tag{8}$$

$$\alpha(\theta_c) = \alpha_{C,0} - \alpha_{C,1}\cos(\theta_c + \theta_{1,\alpha}) - \alpha_{C,2} \cdot \cos(2(\theta_c + \theta_{2,\alpha})), \tag{9}$$

with $\theta_{i,\alpha}$ and $\theta_{i,l}$ being the desired angle of attack and reel-out phase shift, and $l_{t,i}$, $\alpha_{C,i}$ the l_t- and α-Fourier coefficients. The desired angle of attack is fed to the attitude controller described in the following subsection. The desired tether length is processed in the winch controller. A P-controller converts the desired tether length into the desired reel-out speed, which is passed to a PI-controller to determine the desired generator torque.

Additionally to the winch and angle of attack control, the wings spanwise lift distribution can be controlled by the distributed morphing actuators, affecting the longitudinal and lateral dynamics of the aircraft. To keep the number of control parameters tractable, wind speed dependent morphing wing shapes and thus desired spanwise lift distributions are predefined (defined as specific actuation levels for the 18 actuators). Similar to the tether length and the angle of

attack, a Fourier series on the desired flight path of the variable θ_c is then defined, dictating the overall actuation level m_a and thus the morphing wing shape at each operating point in the power cycle. The Fourier series is defined as follows:

$$m_a(\theta_c) = m_{a,0} - m_{a,1}\cos(\theta_c + \theta_{1,m}) - m_{a,2} \cdot \cos(2(\theta_c + \theta_{2,m})). \tag{10}$$

With this approach, wind speed and operating mode dependent wing shapes can be obtained with a small set of predefined input parameters. This is especially beneficial for optimization purpose, as introduced in Section IV.

2. Lateral dynamics

The implemented lateral controller is based on a modified L1 control logic [52], where the aircraft follows the aforementioned circular trajectory on a plane tilted by κ around the y_I-axis. The scheme of the modified L1-control logic with the tilted plane-fixed reference frame (x_P, y_P, z_P) is depicted in Figure 4.

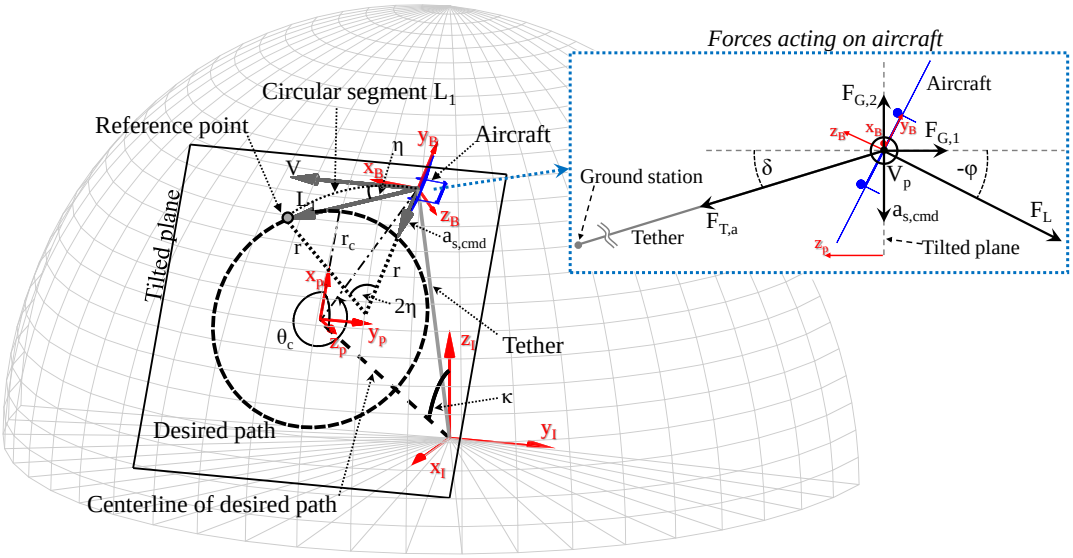

Figure 4 L1-control scheme of the aircraft following a circular trajectory on a tilted plane and desired roll angle ϕ, lateral acceleration command $a_{s,cmd}$, and forces acting on the aircraft.

The L1-control logic of an aircraft flying at velocity V is based on generating a lateral acceleration command by selecting a reference point on the desired path at distance L_1 from the current aircraft position. The acceleration command is derived by calculating the necessary centripetal acceleration to follow a circular segment with radius r and angle η, defined tangential to the velocity vector V of the aircraft:

$$a_{s,cmd} = \frac{V^2}{r} = 2\frac{V^2}{L_1}\sin\eta, \tag{11}$$

where the desired roll angle ϕ to achieve the determined lateral acceleration $a_{s,cmd}$ can be derived by considering the

generated lift F_L, the tether force $F_{T,a}$, and the gravitational force of the aircraft F_G. In the box on the right in Figure 4, the different loads acting on the aircraft in the plane perpendicular to the flight velocity vector V_p projected on the tilted plane are depicted. The lateral acceleration is thus given by:

$$a_{s,cmd} = \frac{1}{m_A}\left(\tan(\delta)F_{G,1} - F_{G,2} + F_L(\tan\delta\cos\phi - \sin\phi)\right), \tag{12}$$

where the angle δ between the tether and the z_p-axis and the gravitational force $F_{G,1}$ and $F_{G,2}$ are functions of the aircraft's state. Additionally knowing the aircraft lift F_L[‡], the equation can be solved for the desired roll angle ϕ.

To convert the desired roll-angle and angle of attack to actuator inputs, a standard cascaded aircraft attitude controller is implemented [53]. The outer loop consists of two PI-controllers, transforming the roll- and incidence angle-error into a desired roll- and pitch-rate. The inner loop, consisting of two P-controllers with variable gains as a function of the flight velocity, transform the desired roll- and pitch-rates to morphing actuation-levels and elevator-angles.

IV. Optimization

To quantify the potential benefit of applying morphing to AWE, the introduced reduced-order model is incorporated into a genetic optimization framework [54]. A high-level objective is defined, namely to maximize the average annual power production of the AWE system. The structural, aerodynamic, flight trajectory, and controls related parameters are optimized concurrently. This increases the complexity of the optimization compared to a sequential approach, but results in the identification of a better-performing individual, due to the possibility of assessing and exploiting interdisciplinary interactions [3]. To quantify the benefit of a concurrent compared to a sequential optimization, two optimizations are performed. First, a sequential optimization comprising of an aero-structural followed by a trajectory and controls optimization is performed. The aero-structural optimization (Opt_{1a}) is not considering the flight dynamics and evaluates the system performance following the approach presented in [13]. After the aero-structural optimization, a trajectory and controls optimization is performed (Opt_{1b}), taking the optimized wing design from Opt_{1a} and using the coupled flight dynamics and aeroelastic model to assess the performance. Second, an optimization concurrently considering the aero-structural, trajectory and controls parameters is conducted (Opt_2). This allows assessing the potential of a complete AWE flight mission concurrent multidisciplinary optimization.

Thereafter, a third optimization is performed, focusing solely on wing shape changes achieved through morphing at different wind speeds and operating modes, quantifying the potential benefit of applying morphing to AWE aircraft (Opt_3). In Opt_3, the optimized wing from the previous Opt_2 is used as a reference and only the morphing related parameters are optimized. This allows assessing the potential benefit of applying morphing to AWE. The three different optimizations are summarized in Table 1.

[‡]It is assumed that the lift is estimated by a five-hole probe measuring the instantaneous angle of attack and flight speed.

Table 1 Optimization runs

Case	Optimization approach
Opt_{1a}	Sequential part a: aero and structure
Opt_{1b}	Sequential part b: trajectory and control
Opt_2	Concurrent: aero, structure, trajectory and control
Opt_3	Full-wing camber-morphing (using wing design Opt_2)

In the following section, the optimization procedure is described in detail. First, the AWE performance evaluation is introduced, followed by the parametrization of the aerodynamic shape, the wing internal structure, composite layup, and the AWE related trajectory and control parameters. Thereafter, the optimization goal and constraints are explained.

A. AWE performance evaluation

In the case of Opt_{1a}, which is not considering the flight dynamics of the aircraft, the performance of the AWE system is evaluated using the model introduced in [13]. The average power P_A produced by the AWE system is calculated by considering the traction phase at theoretical optimal reel-out speed and neglecting the retraction phase, as this strongly dependents upon the followed trajectory. The average power production as a function of the wind speed V_W is therefore calculated as:

$$P_A(V_W) = \frac{2}{27}\,\rho\,A\,\frac{c_L^3}{c_D^2}\,V_W^3\,\cos^3\left(\gamma_{eff}\right)\cdot\eta_m, \tag{13}$$

where A is the wing area, c_L and c_D the lift and effective drag coefficient (considering the drag of the tether [55]), γ_{eff} is the effective elevation angle of the tether (considering the cosine losses), and η_m the losses related to maneuvering and rolling the aircraft into the circular trajectory. The flight speed V at optimal reel-out speed ($V_{\text{ro,opt}} = 1/3 V_W$) is related to the wind speed by: $V = \frac{2}{3}\,\frac{c_L}{c_D}\,V_W\cos(\gamma)$. Thus, the lift and drag coefficient can be calculated using the aeroelastic model to assess the power production of the AWE system at a specific wind speed V_W.

In the case of Opt_{1b}, Opt_2, and Opt_3, the performance of the AWE system is evaluated using the coupled flight dynamics and aeroelastic model, which simulates the aircraft flying circular trajectories and periodically reeling the tether in and out. The generated electric power at wind speed V_W is computed as the product of the torque, angular velocity, and efficiency of the generator and is then integrated over one power production cycle to calculate the average power $P_A(V_W)$.

The power production capability of the system is assessed for both performance measures at three different wind speeds $V_{W,1} = V_{W,min}$, $V_{W,2}$, and $V_{W,3} = V_{W,max}$, with $V_{W,2} = 0.5\cdot(V_{W,1} + V_{W,3})$. The average power is linearly interpolated between $V_{W,1}$, $V_{W,2}$, and $V_{W,3}$ and multiplied with a specific offshore wind speed distribution probability

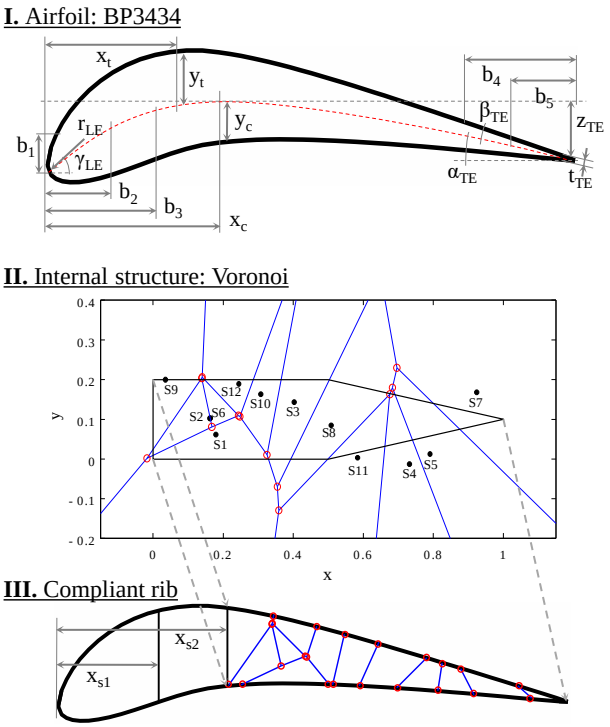

Figure 5 BP3434 undeformed airfoil shape parametrization, Voronoi graph-based compliant rib parametrization, and undeformed airfoil section with compliant rib and spar position parametrization.

f_W [§] (shown in Figure 8 in the results section). The average annual power production $\bar{P}$, which is the objective to be maximized in the optimization, is therefore calculated as:

$$\bar{P} = \sum f_W \cdot P_A(V_W). \tag{14}$$

B. Parametrization

Within the optimization, the algorithm has the freedom to vary a large set of design variables affecting the resulting wing design and flown trajectory. The design variables can be divided in several groups, namely the aerodynamic shape, structure, composite layup, trajectory and control, and morphing-related parameters.

Aerodynamic shape: The aerodynamic shape is defined by the undeformed airfoil and the planform of the wing. The undeformed airfoil shape is defined by a Bezier-PARSEC BP3434 parametrization, an improved Bezier parametrization relying on 15 parameters to represent a large set of airfoils, which is particularly well-suited for strongly cambered high lift airfoils [59, 60]. The parametrization is shown in Figure 5. The airfoil is parametrized at the root and at the tip of the wing and linearly interpolated in between. The planform of the wing is parametrized by the wing span b and by

[§]The wind distribution probability used in this study is the average wind distribution at the locations of all conventional offshore wind parks with a minimum capacity of 200 MW [56, 57]. The rationale for the choice of these locations is that AWE systems placed offshore show greater potential due to the stronger and more uniform winds compared to systems located onshore [58].

bilinearly varying the chord length c from the root over a mid section at b_m to the tip, and the sweep s_m, s_t and twist t_m, t_t at the mid section and tip of the wing, shown in Figure 6.

Structure: The main parameters regarding the wing structure define the compliant ribs and the spars. The truss-like structure of the rib is defined by a Voronoi graph-based parametrization (shown in Figure 5). Its topology provides the required stiffness and affects the deformed shapes of the wing [4, 61]. The main advantages of this parametrization are the small number of variables required to describe the structure, its stability properties (small variable changes lead to small shape changes), and the fact that the obtained structure has no unconnected nodes and segments. With twelve Voronoi-sites $[S_1, ..., S_{12}]$ described by their X and Y coordinate in the rib plane, a total of 24 design variables are used. The wing features nine pairs of ribs per half span, evenly distributed on the wing, as shown in Figure 1, with the same compliant structure at all nine stations. Additionally, the chordwise position of the two spars are defined as design variables: x_{s1}, x_{s2}.

Composite layup: The composite layup ply thickness of the wing skin and spars is parametrized. The parametrization is shown in Figure 6. The wing skin is split in eight sections along the span and in seven sections along the chord (nose, wingbox top and bottom, top rear A and B, bottom rear, and corrugation). The nose and wingbox sections have a $[0°, 90°, \pm 45°]_S$ CFRP UD layup, the spar has a $[\pm 45°]_S$ layup, whereas the rear sections feature a $[0°, 90°]_S$ layup, with the 0° direction defined in spanwise direction. The GFRP corrugated laminate has a predefined thickness of $t_c = 0.6\,\text{mm}$. For the CFRP UD layup, one continuous thickness variable per chordwise section and layup direction is defined at the wing root and wing tip. At the spanwise sections in between the wing root and the wing tip, the thickness is linearly interpolated. This leads to a total of 30 design variables that parametrize the composite layup thickness of the wing. Additionally, stringers are placed along the span between the different sections with a constant thickness and width along the span. The design of the fuselage and stabilizers is taken from the reference aircraft and is kept constant throughout the optimization.

Trajectory and control: The AWE trajectory related parameters and the controller gains are parametrized. The wind speed window in which the system flies is parametrized by $V_{W,min}$ and $V_{W,max}$. The flight path is parametrized by the mean elevation angle $\gamma = 90° - \kappa$ (shown in Figure 4), the radius of the flight circle r_c, and the tether length coefficients of the Fourier series expansion. Furthermore, the angle of attack related Fourier coefficients, the L_1 length and the attitude controller gains are parametrized. The flight path parameters and Fourier coefficients are varied for the three wind speeds ($V_{W,min}$, $V_{W,max}$, and $V_{W,2} = 0.5 \cdot (V_{W,min} + V_{W,max})$), whereas the controller gains are held constant. The tether diameter is not defined as a design variable; its cross-section is sized according to the strength of the wing.

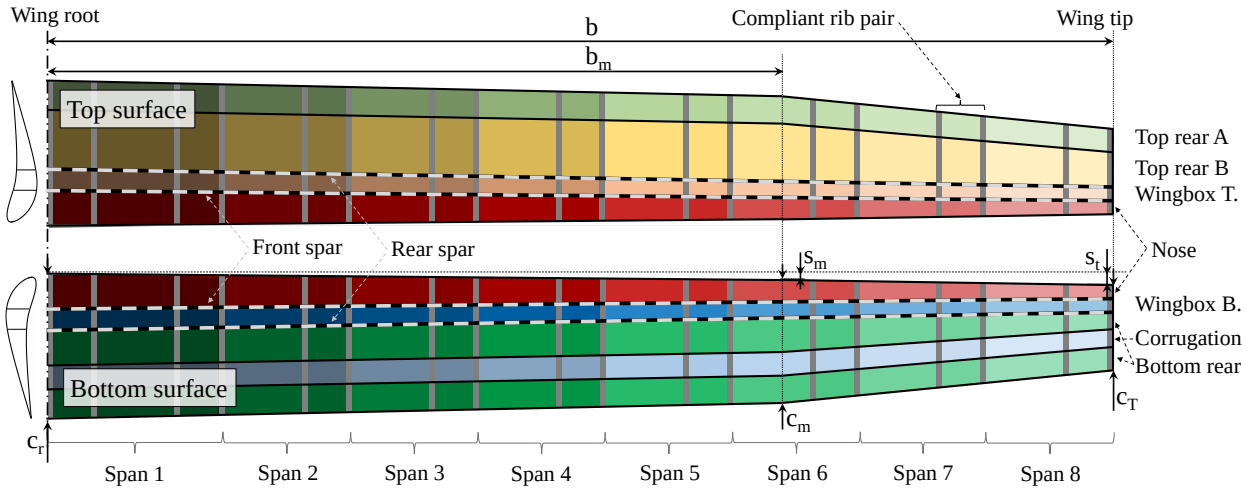

Figure 6 Planform and composite layup thickness parametrization.

Actuator and morphing: The actuator and morphing related parameters are parametrized by the desired maximum actuator forces, which determine the maximum morphing deflections and the actuator weight, given by the relation introduced in [62][¶]. Two parameters define the actuators used for morphing. The first sets the maximum actuator force of the ten innermost actuators. These actuators control the flight condition related shape changes and are additionally used for load alleviation. The second parameter defines the maximum actuator force of the four outermost actuators on the left an right wing. Additionally to alleviating loads and controlling the flight condition related shape changes, these actuators control the roll of the aircraft. For Opt_1 and Opt_2, these two parameters are sufficient to describe the morphing actuation. However, for Opt_3, additionally to the maximum actuator forces, the Fourier coefficients (five parameters) and the spanwise distributed actuation levels (symmetric actuation of the left and right wing, therefore, nine parameters) are defined.

This parametrization leads to a total of 163 design variables, summarized in Table 2.

Table 2 Design variables

Group	#DV	Design variables DV
Aerodynamic shape	39	30 airfoil, 2 span, 3 chord, 2 sweep, 2 twist
Structure & composite layup thickness	56	24 Voronoi, 2 spar position, 28 skin- and 2 spar-thickness
Trajectory & control	52	2 wind speed, 21 flight path, 18 α, 11 controls
Actuator	2	2 max actuator force
Morphing	14	9 actuation level, 5 Fourier coefficient
Total	163	

[¶]The on-board power consumption of the actuators is currently not considered in the optimization. The consequential added weight of an on-board power production systems to allow long endurance power production (e.g. using the VTOL propellers and motors as on board turbines to charge the batteries) or the down time to charge or change the batteries on ground needs to be investigated in future studies.

C. Optimization problem formulation

The objective of the optimization is to maximize the average annual power production of the AWE system. Furthermore, several constraints are included in the optimization. The first requires the final design to withstand the aerodynamic loads without incurring buckling: $\Delta F_\mathrm{b} = 1.5 \cdot F_\mathrm{max} - F_\mathrm{b,crit} \leq 0$. A linear static buckling analysis is conducted to assess the buckling load using Nastran [28]. Preliminary studies of morphing wing designs indicated that buckling initiates failure, whereas strength limitations would occur only at even higher loads. To substantiate this, the maximum stresses of the final wing are assessed, confirming the validity of the assumption. Dynamic aeroelastic instabilities of the wing are considered by constraining the maximum flight speed: $\Delta V_\mathrm{f} = V_\mathrm{max} - V_\mathrm{flutter} \leq 0$. The selected approach to assess the flutter speed V_flutter is based on the assumption of stationary aerodynamics and assumed mode shapes, introduced in [63] and first applied for morphing wings in [17]. The third constraint requires the peak power of each individual to be equal or below 100 kW: $\Delta P_\mathrm{max} = P_\mathrm{max} - 100\,\mathrm{kW} \leq 0$, which is similar to the peak power of state of the art off-grid AWE systems [64]. The fourth constraint aims to ensure a wing design with sufficient morphing capacity, able to alleviate extreme gust loads [65]. In this study, extreme gust loads are defined as a lift increase of 15%. This constraint is expressed by imposing that the lift generated at gust encounter with the wing fully morphed to reduce the lift coefficient has to be smaller or equal than the lift at reference condition without morphing, resulting in the constraint: $\Delta c_\mathrm{L,gust} = 1.15 \cdot c_\mathrm{L,gust} - c_\mathrm{L,ref} \leq 0$. Due to the inviscid nature of the aerodynamic model, a constraint on the maximum lift coefficient needs to be imposed: $\Delta c_\mathrm{L,stall} = c_\mathrm{L,max} - c_\mathrm{L,stall} \leq 0$. The stall lift coefficient $c_\mathrm{L,stall}$ is assessed for each design using the critical section method and XFOIL, as introduced in Section III. Additionally, in the first aero-structural optimization Opt_1a, where the flight dynamics are not considered, a constraint on the minimum achievable rolling moment coefficient is imposed, ensuring sufficient control authority for the subsequent trajectory and controls optimization: $\Delta c_\mathrm{Roll} = c_\mathrm{Roll,max} - c_\mathrm{Roll,crit} \leq 0$. The critical rolling moment coefficient was determined in preliminary studies and is set to $c_\mathrm{Roll,crit} = 0.04$. The problem for the optimization can therefore be formulated as follows:

$$
\begin{aligned}
&\text{maximize} && \mathrm{f}(\mathbf{x}) = \bar{P}(\mathbf{x}) && \mathbf{x} \in \mathbb{R}^{\#\mathrm{DV}} \\
&\text{subject to} && \mathbf{x}_\mathrm{low} \leq \mathbf{x} \leq \mathbf{x}_\mathrm{up} && \mathbf{x}_\mathrm{low},\ \mathbf{x}_\mathrm{up} \in \mathbb{R}^{\#\mathrm{DV}} \\
& && \mathbf{g}(\mathbf{x}) = \left\{ \begin{array}{c} \Delta F_\mathrm{b} \\ \Delta V_\mathrm{f} \\ \Delta P_\mathrm{max} \\ \Delta c_\mathrm{L,gust} \\ \Delta c_\mathrm{L,stall} \\ \Delta c_\mathrm{Roll} \end{array} \right\} \leq 0
\end{aligned}
\tag{15}
$$

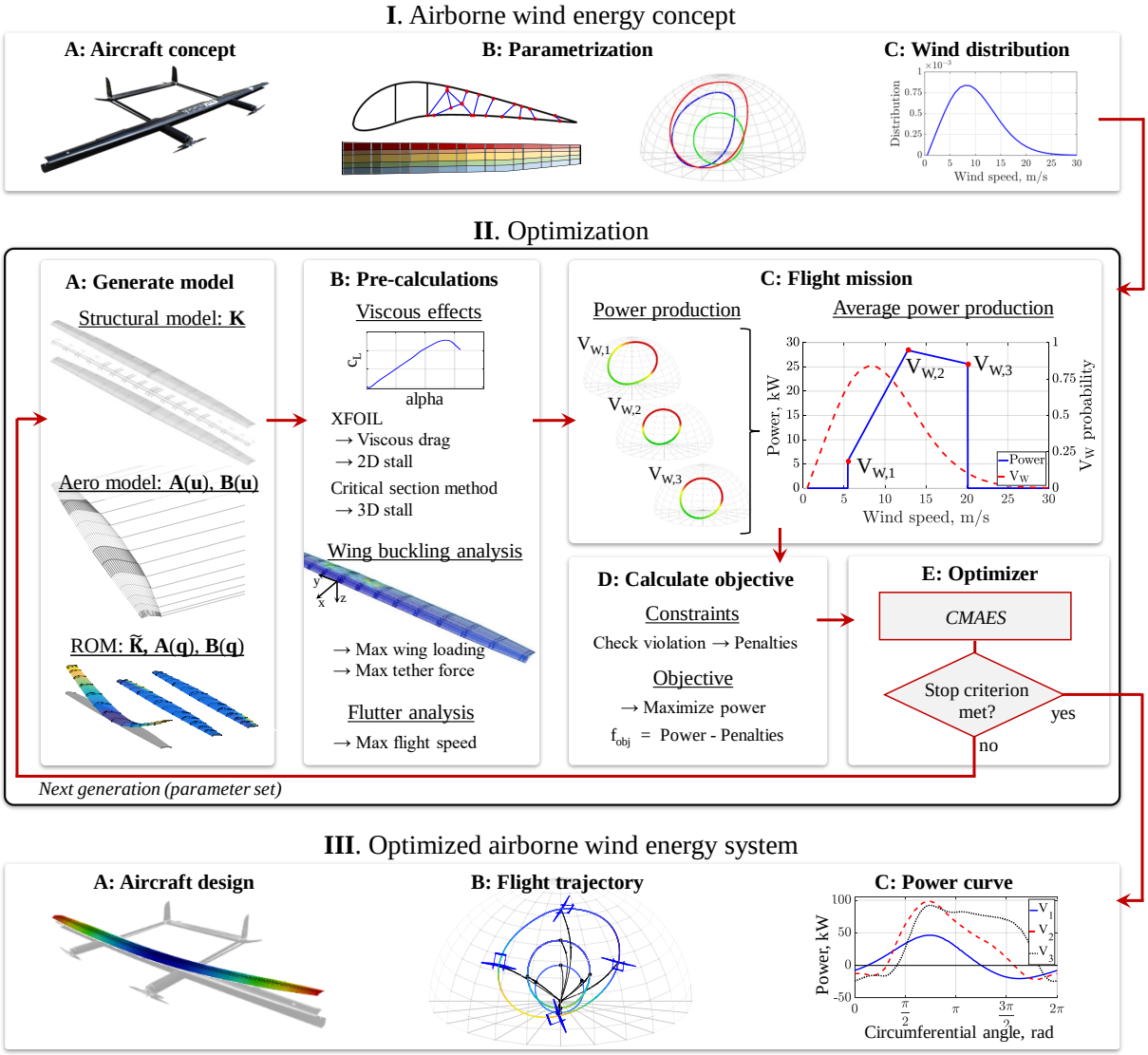

Figure 7 Airborne wind energy morphing wing optimization framework.

The optimization is performed using the algorithm CMA-ES [54], previously used in [4, 13, 18] to optimize morphing wings, as it satisfies the requirements of being able to treat nonsmooth objective functions and of dealing with a large number of design variables. Compared to other genetic algorithms, CMA-ES uses information related to the Hessian of the objective function, adapting the covariance matrix and sampling the search space along a preferential direction, leading to faster convergence [66]. Using inequality constraints would significantly reduce the computational performance of CMA-ES, therefore, the constraints are introduced as penalty terms in the objective function. The framework of the optimization is depicted in Figure 7.

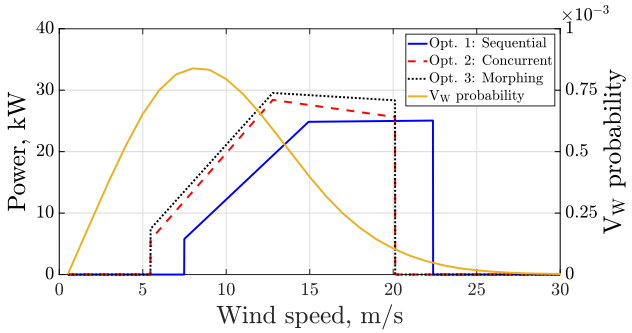

Figure 8 Power over wind speed for the three optimizations and offshore wind speed distribution probability at an altitude of $h = 100$ m.

V. Optimization results

The goal of this study is to assess the potential benefits of running complete flight mission concurrent multidisciplinary optimization and to assess the potential of applying morphing to AWE. Therefore, three optimizations are performed and compared. In Figure 8, the power over wind speed for Opt_1 to Opt_3 and the wind speed distribution probability are shown. Comparing the sequential and the concurrent optimization, the average annual power production increases by 46% from $\bar{P}_{\text{opt1}} = 10.63\,\text{kW}$ to $\bar{P}_{\text{opt2}} = 15.52\,\text{kW}$. By allowing wing shape changes through camber morphing at different flight conditions and operating modes, the power increases by additional 7.8% to $\bar{P}_{\text{opt3}} = 16.73\,\text{kW}$. The main reason for the large increase in power production comparing Opt_1 and Opt_2 can be explained by the fact that the flown trajectory is not considered and that the retraction phase is neglected in the initial aero-structural optimization Opt_{1a}. The increase in power comparing Opt_2 and Opt_3 is due to the distinct wing shapes achieved through morphing at the different flight conditions. The optimizer alternates between decreasing the induced drag and increasing the overall lift coefficient in the traction and retraction phase for different wind speeds, which is only achievable by morphing. In the following subsections, the results are analyzed and discussed in detail. First, the wing design, the flown trajectory, and the performance parameters of the AWE system for Opt_1 and Opt_2 are shown. Afterwards, the performance gain through morphing is discussed by analyzing the distinct wing shapes and aerodynamic properties at different wind speeds and operating modes.

A. Sequential vs. concurrent optimization

In Figure 9, the optimized morphing wing designs are shown. The resulting wing of Opt_1 is shown on the left side of the figure and the wing of Opt_2 is shown on the right side. On the upper part of the figure, the wing planform and composite layup thickness distribution for the different fiber directions of the top and bottom skin and the spar are displayed. On the bottom part of the figure, the airfoil shape with the compliant internal structure, the actuator, and the corrugation is shown.

Several differences between the two resulting wings are worth noting. The wing span and the chord of Opt_1 are

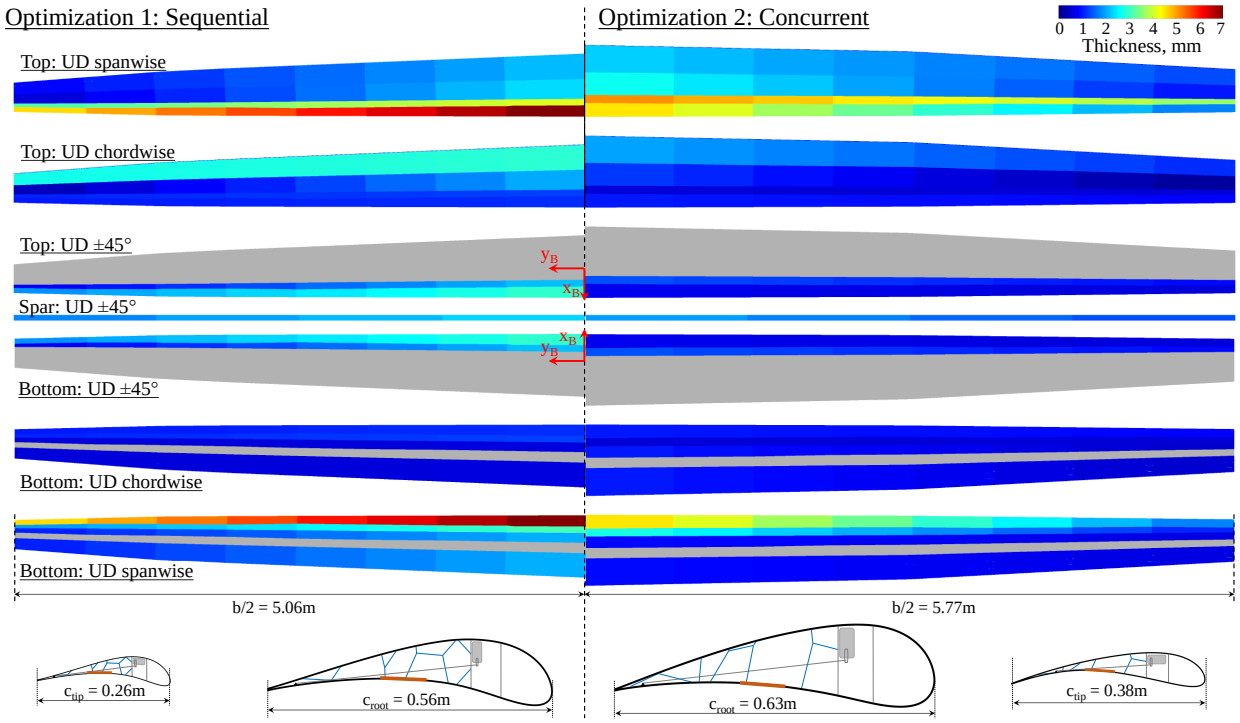

Figure 9 Optimized morphing wing designs for $\mathrm{Opt_1}$ (left) and $\mathrm{Opt_2}$ (right). Top: wing planform and composite layup thickness distribution for the different fiber directions of the top wing surface, the spar, and the bottom wing surface. Bottom: airfoil shapes at the wing root and tip with the respective internal structure (blue), electromechanical actuator (gray), and corrugation (orange).

smaller, resulting in a wing area of $A_{\mathrm{opt1}} = 4.33\,\mathrm{m}^2$ compared to $A_{\mathrm{opt2}} = 6.13\,\mathrm{m}^2$. For both wings, the maximum thickness of the layup is reached at the wing root for the UD layers in spanwise direction. In $\mathrm{Opt_1}$, the maximum is reached in the nose panel with $t_{\mathrm{opt1,max}} = 7.0\,\mathrm{mm}$ and in $\mathrm{Opt_2}$ in the wingbox panel with $t_{\mathrm{opt2,max}} = 5.1\,\mathrm{mm}$. The mass of both wings is similar, with $m_{\mathrm{opt1}} = 93.8\,\mathrm{kg}$ and $m_{\mathrm{opt2}} = 94.5\,\mathrm{kg}$. The mass per actuator is $m_{\mathrm{actOut,opt1}} = 0.79\,\mathrm{kg}$, $m_{\mathrm{actIn,opt1}} = 0.43\,\mathrm{kg}$ and $m_{\mathrm{actOut,opt2}} = 0.89\,\mathrm{kg}$, $m_{\mathrm{actIn,opt2}} = 0.32\,\mathrm{kg}$ for the outer and inner actuators of $\mathrm{Opt_1}$ and $\mathrm{Opt_2}$, respectively. The airfoils of $\mathrm{Opt_1}$ are more cambered and thinner than the airfoils of $\mathrm{Opt_2}$, especially at the root. It can also be noted that the tip airfoil of $\mathrm{Opt_2}$ is comparably thick in the nose, but has a thinner and sharper trailing edge. The maximum lift coefficient is $c_{\mathrm{L,max,opt1}} = 2.08$ and $c_{\mathrm{L,max,opt2}} = 1.93$. The compliant internal structure changes slightly from $\mathrm{Opt_1}$ to $\mathrm{Opt_2}$. In $\mathrm{Opt_1}$, a tighter truss structure is placed behind the rear spar, increasing the stiffness of the rib. The stiffness decreases towards the trailing edge of the airfoil as the amount of trusses is reduced. In $\mathrm{Opt_2}$, the section behind the rear spar is more compliant given the lower truss density, with an increased number of trusses towards the rear, stiffening the trailing edge. The main difference between the two optimized wings is thus the smaller wing area but higher maximum lift coefficient achieved by a more cambered and thinner airfoil of $\mathrm{Opt_1}$. To achieve the required bending stiffness at the wing root with the thinner airfoil of $\mathrm{Opt_1}$, the composite layup thickness needs to be increased.

The reason why the optimizer tends to a smaller wing area and a higher lift airfoil is due to the performance modeling

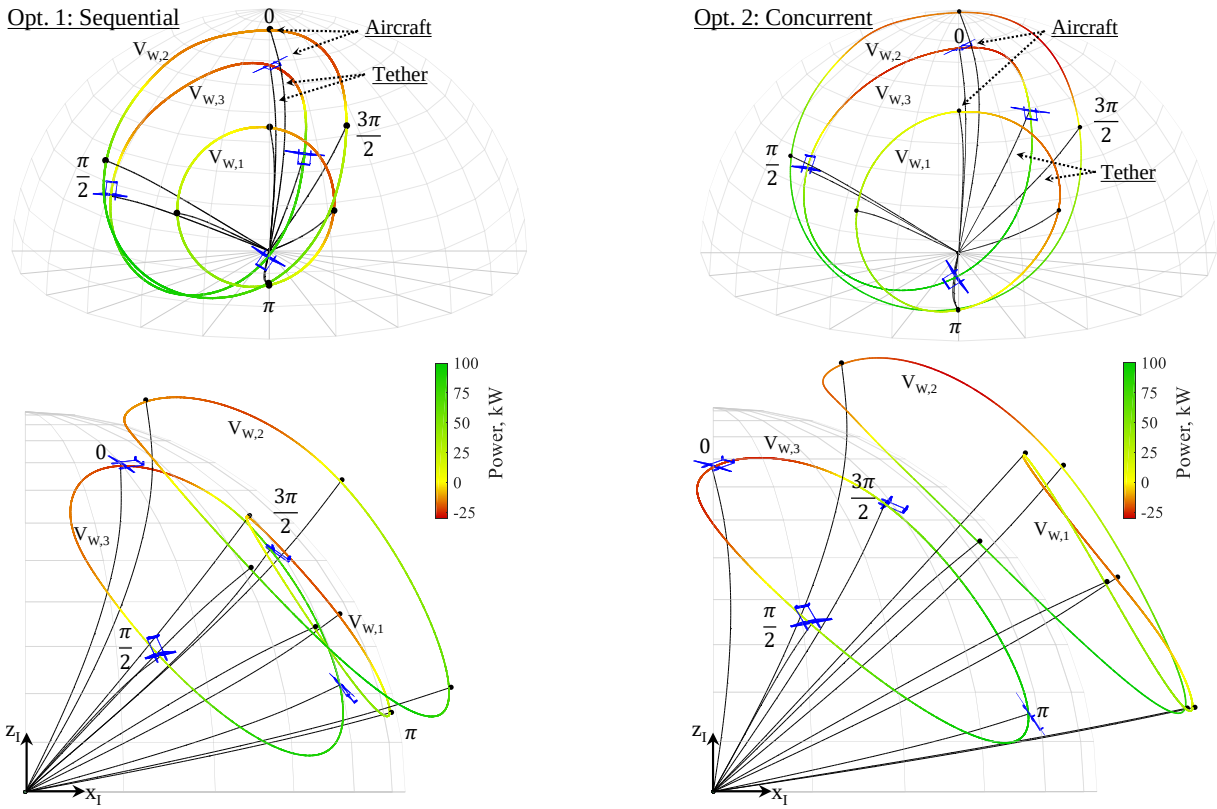

Figure 10 Front and side view of flown trajectory with produced power for Opt_1 (left) and Opt_2 (right). Dimension of sphere for comparison: $r_s = 350$ m.

and the objective function used in Opt_{1a}, as defined in Equation 14, not considering the flown trajectory and neglecting the retraction phase. The objective is therefore mainly maximized by increasing the power harvesting factor c_L^3/c_D^2. In Opt_{1a}, a low wing drag coefficient is thus less important than achieving a higher lift coefficient. Comparing the performance of both wings using the objective function based on Equation 14 ($\bar{P} = \sum(f_W \cdot \frac{2}{27}\rho A \frac{c_L^3}{c_D^2} V_W^3 \cos^3(\gamma_{eff}) \cdot \eta_m)$), the wing of Opt_1 would outperform the wing of Opt_2 by 18%. However, the model assumes a theoretical optimal reel-out speed and is not considering the retraction phase, leading to the large mismatch in power production: considering the optimized flown trajectory, the wing of Opt_2 outperforms the wing of Opt_1 by 46%, highlighting the importance of concurrently considering both disciplines.

In Figure 10, the flown trajectories and the power production for the different wind speeds and optimizations are shown. To better visualize the dynamics, the resulting trajectories, wing deformations and performance parameters are animated and can be found here: **https://polybox.ethz.ch/index.php/s/A0EZxSiKEznPOor**

First, it can be observed that the resulting flight paths of both optimizations are very similar, and second, that the trajectory deviates from the initial circular trajectory for high wind speeds. At the maximum wind speed $V_{W,3}$, a wide path is flown with a high elevation angle $\gamma_{\text{W3,opt1}} = 44.7°$, $\gamma_{\text{W3,opt2}} = 59.2°$ and an average tether length of

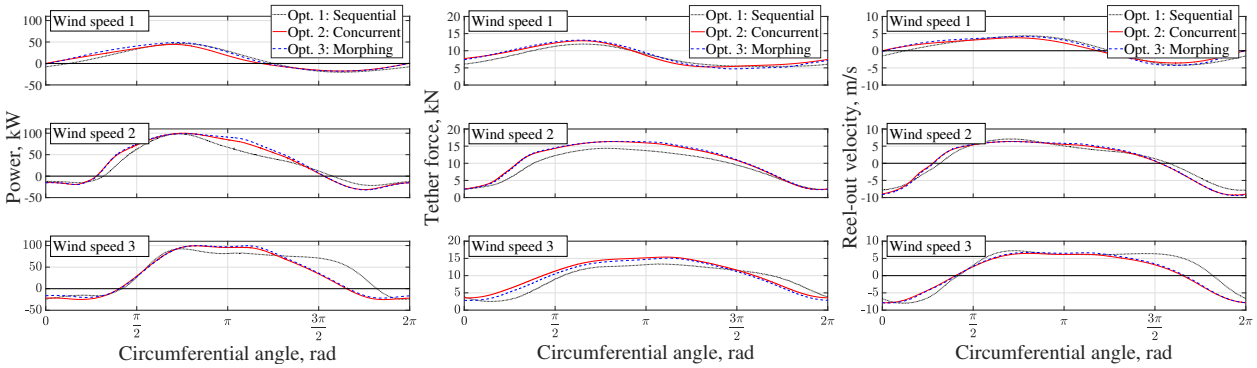

Figure 11 Power production (left), tether force (center), reel-out speed (right) over one power cycle for the different wind speeds and optimizations.

$\bar{l}_{\mathrm{t,opt1}}(V_{W,3}) = 304\,\mathrm{m}$ and $\bar{l}_{\mathrm{t,opt2}}(V_{W,3}) = 298\,\mathrm{m}$. This allows the aircraft to fly almost horizontal and perpendicular to the wind in the retraction phase and thereby minimizing the force acting on the tether and the power to reel-in the aircraft. The low flight speed and high wind speed in the retraction phase becomes apparent in the large tether sag at $\theta = 0$, where the aerodynamic drag of the tether has a significant influence on its dynamics.

In Figure 11, the power production, tether force, and tether reel-out speed over one power cycle for the different optimizations and wind speeds is shown (The results from Opt_3 are also shown in the same plot, but only discussed in the next section). It can be seen that the maximum generator power is not only reached at $V_{W,3}$ but also at $V_{W,2}$. This is achieved by increasing the tether length at $V_{W,2}$ to $\bar{l}_{\mathrm{t,opt1}}(V_{W,2}) = 395\,\mathrm{m}$ and $\bar{l}_{\mathrm{t,opt2}}(V_{W,2}) = 433\,\mathrm{m}$, thereby reaching higher altitudes characterized by stronger winds. At $V_{W,1}$, the flown trajectory is almost circular and the elevation angle is reduced to $\gamma_{\mathrm{W1,opt1}} = 29.6°$ and $\gamma_{\mathrm{W1,opt2}} = 28.0°$, as a result of the reduced tether force needed to reel in the aircraft at lower wind speeds. On the bottom of Figure 10, the reeling in and out of the tether is shown. The traction phase is initiated at $\theta \approx \pi/4$ and ends at $\theta \approx 3\pi/2$, also shown in Figure 11, where the reel-out velocity is depicted. It should be noted that the wind speed at which the system is operated is an optimization parameter. This can be seen in Figure 8: the sequentially optimized system is operated at higher wind speeds than the concurrently optimized system. Therefore, even though the power curves shown in Figure 11 are similar for the concurrently and sequentially optimized systems, the average annual power production is significantly higher for the concurrently optimized system, given the specific wind speed distribution probability.

The shown results highlight the potential of the introduced optimization framework and the impact of conducting a concurrent multidisciplinary optimization, with an improved average annual power production of the morphing AWE system of 46% using the concurrent aeroservoelastic optimization compared to the sequential optimization.

B. Morphing optimization

The third optimization is performed to assess the potential of allowing wing shape changes through morphing at different wind speeds and operating modes. The optimizer is only allowed to vary the morphing related parameters (14 morphing parameters from Table 2). The optimized wing, the flown trajectory, and the controls parameters are taken from Opt_2 and are kept constant. At each wind speed, one optimization is performed. In Figure 12 on the left, the resulting spanwise trailing edge displacement (TED) by morphing the wing over one power cycle for different wind speeds is shown. The induced change in spanwise lift coefficient is shown in Figure 12 on the right. Furthermore, in Figure 11 and in Figure 13, the performance of the morphing wing is compared to the wing from Opt_2.

The increase in power production achieved through morphing with respect to Opt_2 for the three wind speeds is 31.6%, 4.0%, and 10.6%. In total, this accounts for an increase in average power production of 7.8%. This is mainly achieved by adapting the lift distribution towards the wingtip, compromising aerodynamic efficiency for higher lift or vice versa. At the lowest wind speed $V_{W,1}$, the biggest potential to increase the power production is found, as the maximum power and tether force constraints are not active at this wind speed. Therefore, in the traction phase, the optimizer increases the camber of the wing towards the tip, leading to a less efficient lift distribution and a larger induced drag, but increasing the power production owing to the larger total lift coefficient. In the retraction phase, the lift coefficient towards the wingtip is decreased, increasing the efficiency by decreasing the induced drag. Thereby, the tether force is decreased and the retraction is facilitated. At $V_{W,2}$, no large adjustments and power gains are possible. The power produced at this wind speed has the largest influence on the objective of the reference optimization. Therefore, the reference optimization already defines a well performing wing shape at this wind speed. Additionally, the tether force and power constraint are active in the traction phase, therefore only little power can be gained. Nevertheless, a power gain is achieved in the final part of traction phase (between $\theta \approx \pi$ and $\theta \approx {}^{3\pi}/_{2}$) by increasing the lift coefficient over a large section of the wing. At the highest wind speed $V_{W,3}$, large potential in increasing the power production is found in the retraction phase by reducing the lift coefficient and the induced drag. Thereby, the force on the tether is decreased, which can be seen in Figure 11 and 13.

Overall, the optimization results are very promising, showing the potential of applying morphing to AWE to achieve distinct wing shapes and aerodynamic properties at different wind speeds and operating modes.

VI. Conclusion

This study presents an accurate and tractable reduced-order aeroelastic and flight dynamics model allowing to run complete flight mission multidisciplinary design optimization of morphing wings. The framework is demonstrated on a morphing wing AWE system. The model of the AWE system couples a generator-, a tether-, and a flight dynamics-model with a 3-D panel method-based CFD and a 3-D structural finite element model of a morphing wing. Model order reduction techniques are applied to the structural and aerodynamic model of the wing, drastically increasing the

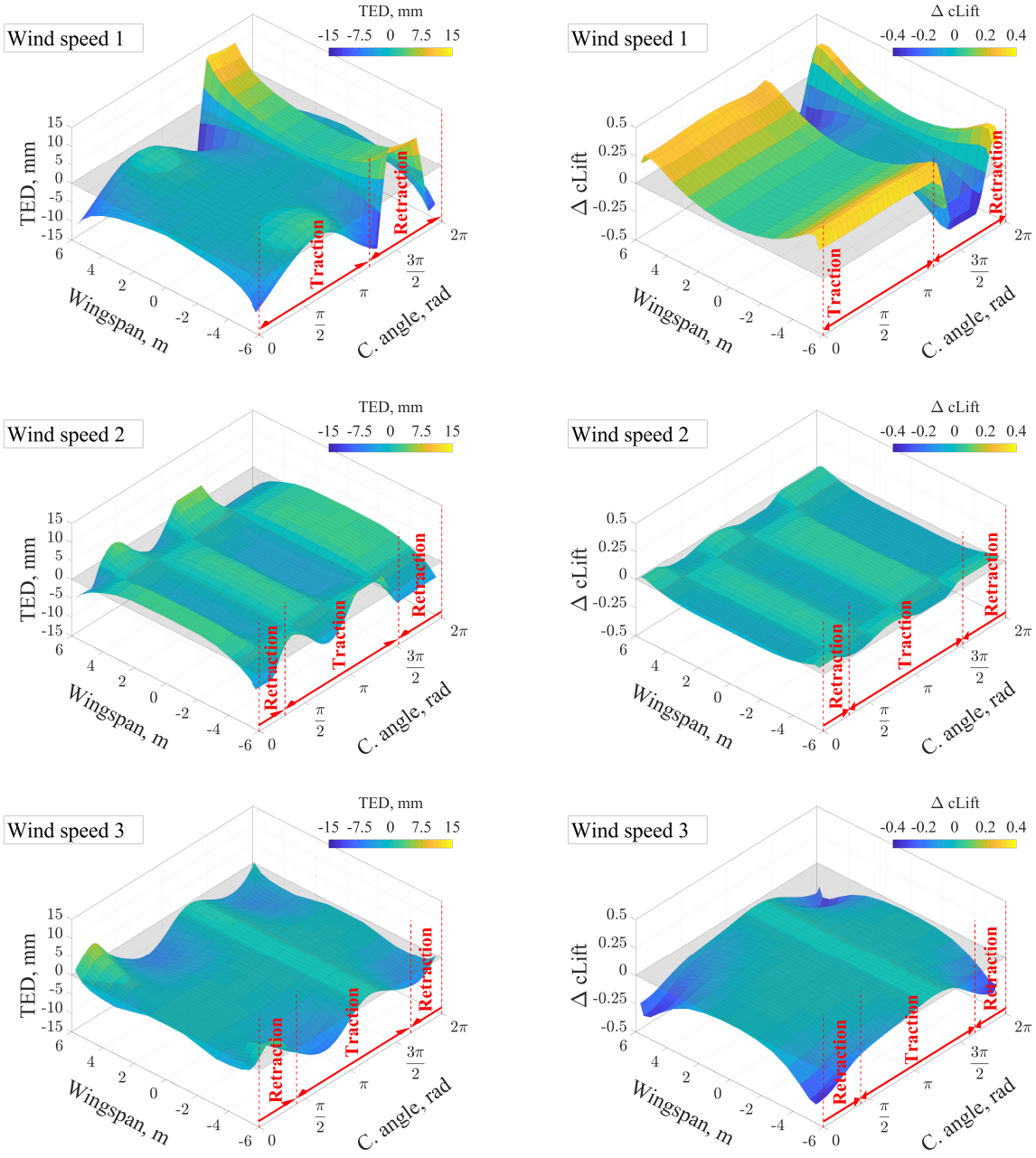

Figure 12 Left: morphing induced spanwise trailing edge displacement (TED) and right: spanwise distribution of morphing induced lift coefficient change (ΔcLift = $cLift_{Opt3} - cLift_{Opt2}$) over one power cycle for different wind speeds.

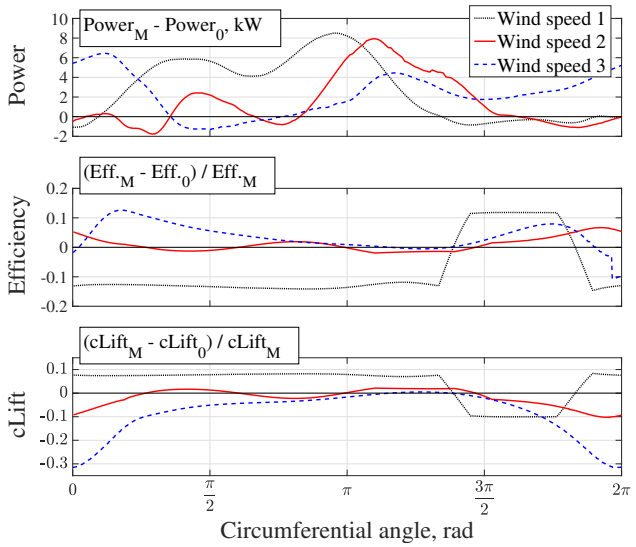

Figure 13 Performance comparison of morphing (subscript M, Opt_3) vs. reference wing (subscript 0, Opt_2). Delta power (top), normalized delta efficiency (lift over drag coefficient, center), normalized delta lift coefficient (bottom) over one power cycle for different wind speeds.

computational efficiency of the simulation environment. A speed-up factor of 180 is achieved at virtually no decrease in accuracy, allowing tractable optimization using the proposed model.

Aeroservoelastic optimizations are conducted, concurrently optimizing the aerodynamic, structural, trajectory and controls related parameters of the camber-morphing AWE system. The results show the potential of the introduced reduced-order model and of the multidisciplinary optimization framework: the model is able to analyze the aeroelastic and flight dynamic behavior of a morphing wing AWE system in great detail and the optimization framework allows to concurrently optimize a complete AWE system exploiting interdisciplinary interactions. The potential of the optimization is demonstrated comparing the concurrent with a sequential optimization approach, increasing the average power production of the AWE system by 46%.

Furthermore, the potential of applying morphing to increase the power production of an AWE system by achieving distinct wing shapes and aerodynamic properties at different wind speeds and operating modes is demonstrated. At low wind speeds, large power production gains in the traction phase can be achieved by increasing the lift towards the wingtip, compromising aerodynamic efficiency for increased lift and therefore tether force. At high wind speeds, large power production gains can be achieved by morphing through reducing the induced drag and tether force in the retraction phase. Overall, a 7.8% increase in average power production through morphing can be achieved. Given the increase in power production by using the concurrent optimization strategy and by using camber-morphing over the full wing span, future studies should investigate the combination of both aspects. By concurrently optimizing all design parameters including morphing to change the wing characteristics at different flight conditions and operating modes, a further power production increase could potentially be achieved.

In this study, the morphing wing reduced-order modeling and optimization framework is demonstrated on an AWE system. However, the framework is applicable to any other flight system where performance gains can be envisioned by introducing morphing. The large benefit compared to existing morphing wing optimization frameworks is that complete flight missions can be considered using a detailed structural model of the morphing mechanism, thus, allowing to truly quantify the potential benefits of morphing wings.

References

[1] Barbarino, S., Bilgen, O., Ajaj, R. M., Friswell, M. I., and Inman, D. J., "A Review of Morphing Aircraft," *Journal of Intelligent Material Systems and Structures*, Vol. 22, No. June, 2011.

[2] Li, D., Zhao, S., Ronch, A. D., Xiang, J., Drofelnik, J., Li, Y., Zhang, L., Wu, Y., Kintscher, M., Peter, H., Rudenko, A., Guo, S., Yin, W., Kirn, J., Storm, S., and Breuker, R. D., "A review of modelling and analysis of morphing wings," *Progress in Aerospace Sciences*, Vol. 100, No. May, 2018, pp. 46–62.

[3] Molinari, G., Quack, M., Dmitriev, V., Morari, M., Jenny, P., and Ermanni, P., "Aero-Structural Optimization of Morphing Airfoils for Adaptive Wings," *Journal of Intelligent Material Systems and Structures*, Vol. 22, No. 10, 2011, pp. 1075–1089.

[4] Molinari, G., Arrieta, A. F., and Ermanni, P., "Aero-Structural Optimization of Three-Dimensional Adaptive Wings with Embedded Smart Actuators," *AIAA Journal*, Vol. 52, No. 9, 2014, pp. 1940–1951.

[5] Previtali, F., Arrieta, A. F., and Ermanni, P., "Investigation of the optimal elastic and weight properties of passive morphing skins for camber-morphing applications," *Smart Materials and Structures*, Vol. 25, No. 5, 2016.

[6] Woods, B. K. and Friswell, M. I., "Multi-objective geometry optimization of the Fish Bone Active Camber morphing airfoil," *Journal of Intelligent Material Systems and Structures*, Vol. 27, No. 6, 2016, pp. 808–819.

[7] Keidel, D., Molinari, G., and Ermanni, P., "Aero-structural optimization and analysis of a camber-morphing flying wing: Structural and wind tunnel testing," *Journal of Intelligent Material Systems and Structures*, Vol. 30, No. 6, 2019, pp. 908–923.

[8] Burdette, D. A., Kenway, G. K., and Martins, J. R., "Aerostructural design optimization of a continuous morphing trailing edge aircraft for improved mission performance," *17th AIAA/ISSMO Multidisciplinary Analysis and Optimization Conference*, No. June, 2016, pp. 1–16.

[9] Burdette, D. A. and Martins, J. R., "Design of a transonic wing with an adaptive morphing trailing edge via aerostructural optimization," *Aerospace Science and Technology*, Vol. 81, 2018, pp. 192–203.

[10] Burdette, D. A. and Martins, J. R. R. A., "Impact of Morphing Trailing Edges on Mission Performance for the Common Research Model," *Journal of Aircraft*, Vol. 56, No. 1, 2019.

[11] Ahrens, U., Diehl, M., and Schmehl, R., *Airborne Wind Energy*, Springer, 2014.

[12] Loyd, M. L., "Crosswind Kite Power," *Journal of Energy*, Vol. 4, No. 3, 1980, pp. 106–111.

[13] Fasel, U., Keidel, D., Molinari, G., and Ermanni, P., "Aerostructural optimization of a morphing wing for airborne wind energy applications," *Smart Materials and Structures*, Vol. 26, No. 9, 2017.

[14] Fasel, U., Tiso, P., Keidel, D., Molinari, G., and Ermanni, P., "Reduced-Order Dynamic Model of a Morphing Airborne Wind Energy Aircraft," *AIAA Journal*, 2019, pp. 1–13.

[15] Affentranger, L., Baumann, L., Canonica, R., Gehri, I., König, G., Mattia, C., Michalski, A., Wiesemüller, F., Wild, O., Fasel, U., Keidel, D., Molinari, G., and Ermanni, P., "ftero - On the Development of an Airborne Wind Energy System," *Airborne Wind Energy Conference*, 2017.

[16] Keidel, D., Fasel, U., Baumann, L., Molinari, G., and Ermanni, P., "Experimental Validation of a Morphing Wing for Airborne Wind Energy Applications," *28th International Conference on Adaptive Structures and Technologies, Cracow, Poland*, 2017.

[17] Molinari, G., Quack, M., Arrieta, A. F., Morari, M., and Ermanni, P., "Design, Realization and Structural Testing of a Compliant Adaptable Wing," *Smart Materials and Structures*, Vol. 24, No. 10, 2015.

[18] Keidel, D., Fasel, U., Molinari, G., and Ermanni, P., "Design, Development, and Structural testing of a Camber-Morphing Flying Wing Airplane," *Conference on Smart Materials, Adaptive Structures and Intelligent Systems*, ASME, Snowbird, UT, USA, 2017.

[19] Thill, C., Etches, J. A., Bond, I. P., Potter, K. D., and Weaver, P. M., "Composite corrugated structures for morphing wing skin applications," *Smart Materials and Structures*, Vol. 19, No. 12, 2010.

[20] Previtali, F., Arrieta, A. F., and Ermanni, P., "Double-walled corrugated structure for bending-stiff anisotropic morphing skins," *Journal of Intelligent Material Systems and Structures*, Vol. 26, No. 5, 2014, pp. 599–613.

[21] Waszak, M. R. and Schmidt, D. K., "Flight dynamics of aeroelastic vehicles," *Journal of Aircraft*, Vol. 25, No. 6, 1988, pp. 563–571.

[22] Schmidt, D. K. and Raney, D. L., "Modeling and Simulation of Flexible Flight Vehicles," *Journal of Guidance, Control, and Dynamics*, Vol. 24, No. 3, 2001, pp. 539–546.

[23] Katz, J. and Plotkin, A., *Low-Speed Aerodynamics*, McGraw-Hill, New York, 2nd ed., 2001.

[24] Filkovic, D., *Graduate Work*, Thesis report, University of Zagreb, 2008.

[25] Molinari, G., Arrieta, A. F., Guillaume, M., and Ermanni, P., "Aerostructural Performance of Distributed Compliance Morphing Wings: Wind Tunnel and Flight Testing," *AIAA Journal*, Vol. 54, No. 12, 2016, pp. 3859–3871.

[26] Kress, G. and Winkler, M. C., "Corrugated laminate homogenization model," *Composite Structures*, Vol. 92, No. 3, 2010, pp. 795–810.

[27] Winkler, M. C., *Analysis of corrugated laminates*, Ph.D. thesis, ETH Zurich, 2012.

[28] MSC Software Corporation, "MSC Nastran Linear Static Analysis User's Guide," 2014.

[29] Besselink, B., Tabak, U., Lutowska, A., Van De Wouw, N., Nijmeijer, H., Rixen, D. J., Hochstenbach, M. E., and Schilders, W. H., "A comparison of model reduction techniques from structural dynamics, numerical mathematics and systems and control," *Journal of Sound and Vibration*, Vol. 332, 2013, pp. 4403–4422.

[30] Géradin, M. and Rixen, D. J., *Mechanical Vibrations: Theory and Application to Structural Dynamics*, Wiley, 3rd ed., 2015.

[31] Anderson, J. D., *Fundamentals of Aerodynamics*, McGraw-Hill Science/Engineering/Math, 3rd ed., 2001.

[32] Drela, M. and Gilest, M. B., "Viscous-Inviscid Analysis of Transonic and Low Reynolds Number Airfoils," *AIAA Journal*, Vol. 25, No. 10, 1987, pp. 1347–1355.

[33] Drela, M., "XFOIL," `http://web.mit.edu/drela/Public/web/xfoil/`, 2008.

[34] Singh, B., *A Medium-Fidelity Method for Rapid Maximum Lift Estimation*, Thesis report, TU Delft, 2017.

[35] Abbott, I. H. and Von Doenhoff, A. E., *Theory of Wing Sections: Including a Summary of Airfoil data*, Dover Publications, 1959.

[36] Miller, K. S., "On the Inverse of the Sum of Matrices," *Mathematics Magazine*, Vol. 54, No. 2, 1981, pp. 67–72.

[37] Harder, R. L. and Desmarais, R. N., "Interpolation using surface splines." *Journal of Aircraft*, Vol. 9, No. 2, 1972, pp. 189–191.

[38] Duchon, J., "Splines Minimizing Rotation-Invariant Semi-Norms in Sobolev Spaces," *Constructive Theory of Functions of Several Variables*, 1976.

[39] de Boer, A., van Zuijlen, A. H., and Bijl, H., "Review of coupling methods for non-matching meshes," *Computer Methods in Applied Mechanics and Engineering*, Vol. 196, No. 8, 2007, pp. 1515–1525.

[40] Shepard, D., "A two-dimensional interpolation function for irregularly-spaced data," *Proceedings of the 1968 ACM national conference*, 1968, pp. 517–524.

[41] Lonsain, J., *Aeroelastic analysis of a 3D wing structure with a flexible trailing edge*, Thesis report, TU Delft, 2017.

[42] Zipfel, P. H., *Modeling and Simulation of Aerospace Vehicle Dynamics*, 2007.

[43] Fechner, U., van der Vlugt, R., Schreuder, E., and Schmehl, R., "Dynamic model of a pumping kite power system," *Renewable Energy*, Vol. 83, 2015, pp. 705–716.

[44] Schreuder, E., *Improving winch control performance in Kite Power Systems using gain scheduling and compliant element*, Ph.D. thesis, TU Delft, 2013.

[45] Burton, T., Sharpe, D., Jenkins, N., and Bossanyi, E., *Wind energy handbook*, John Wiley & Sons Ltd., 2001.

[46] Galliard, C. M., *Spherical Guidance and Control for an Airborne Wind Energy System*, Thesis report, ETH Zurich, 2017.

[47] Goldstein, L., "Density of Individual Airborne Wind Energy Systems in AWES Farms," 2014.

[48] Kruijff, M. and Ruiterkamp, R., "A roadmap towards airborne wind energy in the utility sector," *Airborne Wind Energy, Green Energy and Technology*, Springer Nature Singapore Pte Ltd, 2018.

[49] Licitra, G., *Identification and Optimization of an Airborne Wind Energy System*, Ph.D. thesis, Universität Freiburg, 2018.

[50] Fagiano, L., Nguyen-Van, E., Rager, F., Schnez, S., and Ohler, C., "Autonomous Takeoff and Flight of a Tethered Aircraft for Airborne Wind Energy," *IEEE Transactions on Control Systems Technology*, Vol. 26, No. 1, 2018, pp. 151–166.

[51] Rapp, S., Schmehl, R., Oland, E., Smidt, S., Haas, T., and Meyers, J., "A Modular Control Architecture for Airborne Wind Energy Systems," *AIAA SciTech Forum*, 2019.

[52] Park, S., Deyst, J., and How, J., "A New Nonlinear Guidance Logic for Trajectory Tracking," *AIAA Guidance, Navigation, and Control Conference and Exhibit*, 2004.

[53] Meier, L., Honegger, D., and Pollefeys, M., "PX4: A node-based multithreaded open source robotics framework for deeply embedded platforms," *ICRA (Int. Conf. on Robotics and Automation)*, 2015.

[54] Hansen, N. and Ostermeier, A., "Completely Derandomized Self-Adaptation in Evolution Strategies," *Evolutionary Computation*, Vol. 9, No. 2, 2001, pp. 159–195.

[55] Houska, B. and Diehl, M., "Optimal Control for Power Generating Kites," *European Control Conference*, 2007, pp. 3560–3567.

[56] Global Wind Atlas, "http://globalwindatlas.com/," 2016.

[57] Offshore Wind Farms, "https://en.wikipedia.org/wiki/List_of_offshore_wind_farms," 2016.

[58] Fagiano, L., Milanese, M., Razza, V., and Gerlero, I., "Offshore High-Altitude Wind Energy Using Controlled Airfoils," *European Wind Energy Conference (EWEC)*, 2010.

[59] Rogalsky, T., *Acceleration of Differential Evolution for Aerodynamic Design*, Ph.D. thesis, University of Manitoba, 2004.

[60] Derksen, R. W. and Rogalsky, T., "Bezier-PARSEC: An optimized aerofoil parameterization for design," *Advances in Engineering Software*, Vol. 41, 2010, pp. 923–930.

[61] Hamda, H., Jouve, F., Evelyne, L., Schoenauer, M., and Sebag, M., "Compact Unstructured Representations for Evolutionary Design," *Applied Intelligence*, Vol. 16, No. 2, 2002, pp. 139–155.

[62] Previtali, F., Arrieta, A. F., and Ermanni, P., "Performance of a Three-Dimensional Morphing Wing and Comparison with a Conventional Wing," *AIAA Journal*, Vol. 52, No. 10, 2014, pp. 2101–2113.

[63] Hodges, D. H. and Pierce, G. A., *Introduction to Structural Dynamics and Aeroelasticity*, Cambridge University Press, 2002.

[64] Cherubini, A., Papini, A., Vertechy, R., and Fontana, M., "Airborne Wind Energy Systems : A review of the technologies," *Renewable and Sustainable Energy Reviews*, Vol. 51, 2015, pp. 1461–1476.

[65] International Electrotechnical Commission, "IEC 61400-1," 2005.

[66] Igel, C., Hansen, N., and Roth, S., "Covariance Matrix Adaptation for Multi-objective Optimization," *Evolutionary Computation*, Vol. 15, No. 1, 2007, pp. 1–28.